Master's thesis

NTNU
Norwegian University of Science and Technology
Faculty of Engineering
Department of Civil and Environmental Engineering

Tianshu Liu

Numerical Study of Air Flow in Air Cavities for Pitched Wooden Roofs

Master's thesis in Civil and Environmental Engineering
Supervisor: Tore Kvande
September 2020

NTNU
Norwegian University of Science and Technology

Tianshu Liu

Numerical Study of Air Flow in Air Cavities for Pitched Wooden Roofs

Master's thesis in Civil and Environmental Engineering
Supervisor: Tore Kvande
September 2020

Norwegian University of Science and Technology
Faculty of Engineering
Department of Civil and Environmental Engineering

NTNU
Norwegian University of
Science and Technology

Preface

The present thesis is the final section of my study of Master Program in Civil and Environmental Engineering at Norwegian University of Science and Technology (NTNU). The topic of the thesis is interdisciplinary that the theory and concepts of building technology and computational fluid dynamics are nicely combined. The work carried out in the past six months has been challenging and exciting and I am very motivated and enjoyed learning new approaches of numerical simulation as well as new knowledge in the field of roof technology.

I would like to thank my academic supervisor Professor Tore Kvande for giving me the opportunity to work on this topic, for his valuable guidance and the inspiring discussions. I appreciate Dr. Lars Gullbrekken's very helpful suggestions and comments. Finally, I thank my family for their endless love, support, and encouragement throughout my study at NTNU.

Trondheim, September 2020

Tianshu Liu

Abstract

In Norway, detached houses and other types of residential small houses with pitched wooden roofs are commonly seen. Ventilated pitched wooden roofs with an air cavity beneath the roofing are of importance for keeping dry conditions for the roof construction and keeping the low temperature to avoid snowmelt on the roof. The airflow passing through the ventilation layer of the roofs is complicated because of various factors to be considered, such as natural convection induced by the temperature difference of insulation surface and roofing, the pitch angle of the roof, the surface roughness of tile battens, etc. To have a better understanding of the flow phenomenon of the air cavity of pitched wooden roofs and to improve the performance of the ventilated pitched roof, for instance with low flow resistance, this thesis explores the airflow behavior by Computational Fluid Dynamics (CFD) simulations.

Following the laboratory model that has been developed and experimentally tested in the NTNU and SINTEF Byggforsk, more than 40 CFD simulations are designed and performed in the present work. Both horizontal and pitched channel flow without and with tile battens are studied and the important factors that may affect the pressure gradient and flow friction are investigated. In the simulations, the flow speed is ranging from 0.02 m/s to 0.8 m/s. The pitch angle is from 0^{o} to 60^{o}. Two temperature differences between the insulation surface and roofing are chosen as 2 K and 10 K. Moreover, the height of the air gap is carefully examined from 0.023 m to 0.14 m. With the adoption of O-block mesh, the simulations with different shapes of round-edged tile battens are carried out. The roundness of tile batten is controlled by adjusting the radius of the tile batten's corner, which is from r = 0.004 m to 0.012 m.

The numerical results are in accordance with theoretical and experimental data, which reveals that the numerical approach is reliable. The CFD results show that the pressure gradient monotonically reduces as the air gap grows. Similarly, the friction coefficient and local loss coefficient are monotonically attenuated with increasing the air gap. The reduction is significant from the air gap 0.023 m to 0.048 m and then the reduction level is weakened from 0.048 m to 0.14 m. On the other hand, regarding the effect of tile batten roundness, the pressure gradient monotonically decreases as the roundness grows, i.e. the radius of round corner increases. As for the friction coefficient and local loss coefficient, the increase of tile batten roundness (the radius of the tile batten corner) attenuates the friction and local loss coefficient. The reduction is most significant from a sharp-edged case to a slightly round-edged case.

As a summary, these numerical findings obtained in the present thesis, in the view of flow resistance reduction, show that increasing the air gap is an effective approach, which works efficiently for the air-gap height from about 0.023 to 0.048 m in the parameter-range considered in the present work. Moreover, utilizing round-edged tile battens in ventilated pitched roofs is another efficient way to reduce the airflow friction, in another word, to increase the flow rate with the same flow conditions. Surprisingly, a slight roundness (r = 0.004 m) leads to a significant reduction of flow friction (about 20%). Therefore, this finding suggests that the slightly round-edged tile batten, which is relatively easy to produce compared with the most round-edged case (r = 0.012 m), might be sufficient in practical application of ventilated pitched wooden roofs.

Sammendrag

I Norge sees ofte eneboliger og andre typer småhus med skrå tretak. Luftede skrå tretak med et lufthulrom under takets tekning er av betydning for å sikre tørre forhold for takkonstruksjonen og samtidig holde lav temperatur for å unngå snøsmelting på taket. Luftstrømningen som går gjennom takets ventilasjonslag er komplisert på grunn av ulike faktorer som må tas i betraktning, for eksempel naturlig konveksjon indusert av temperaturforskjellen mellom isolasjonsoverflaten og taktekkingen, takvinkelen på taket, overflateruheten av steinlekter osv. For å få en bedre forståelse av strømningsforholdene i lufthulromet til skrå tretak og for å forbedre ytelsen til det luftede taket, for eksempel ved lav strømningsmotstand, utforsker denne avhandlingen oppførselen til luftstrømningen ved hjelp av Computational Fluid Dynamics (CFD) simuleringer.

Basert på en laboratoriemodell som er utviklet og testet eksperimentelt ved NTNU og SINTEF Byggforsk, er mer enn 40 CFD-simuleringer designet og utført i det nåværende arbeidet. Både horisontal og stigende kanalstrømning studeres både uten og med steinlekter, og viktige faktorer som kan påvirke trykkgradienten og strømningsfriksjonen blir undersøkt. I simuleringene er strømningshastigheten variert fra 0,02 m/s til 0,8 m/s. Stigningsvinkelen er fra 0^o til 60^o. To temperaturforskjeller mellom isolasjonsoverflaten og taktekkingen, 2 K og 10 K, er studert. Dessuten undersøkes høyden på luftspalten nøye fra 0,023 m til 0,14 m. Simuleringene med et såkalt «O-block mesh» gjennomføres for forskjellige former av rundkantet steinlekter. Rundheten av steinlekten ivaretas ved å tilpasse radien til hjørnet av steinlekten, som er fra r = 0,004 m til 0,012 m.

De numeriske resultatene er i samsvar med teoretiske og eksperimentelle data, som dermed bekrefter at den numeriske tilnærmingen er pålitelig. CFD-resultatene viser at trykkgradienten reduseres monotont når luftspalten øker. På samme måte reduseres friksjonskoeffisienten og den lokale tapskoeffisienten monotont med økende luftspalte. Reduksjonen er betydelig for luftspalter fra 0,023 m til 0,048 m, og deretter avtar reduksjonsgraden fra 0,048 m til 0,14 m. På den andre siden, når det gjelder effekten av den rundkantete steinlekten, reduseres trykkgradienten monotont når rundheten øker, d.v.s. når radiusen til det runde hjørnet øker. Når det gjelder friksjonskoeffisienten og den lokale tapskoeffisienten, demper økningen av steinlektenes rundhet (radius på hjørnet til steinlekten) friksjonen og den lokale tapskoeffisienten. Reduksjonen er mest betydelig fra et rettkantet hjørne til et litt avrundet hjørne.

Oppsummert viser de numeriske funnene oppnådd i denne avhandlingen, med tanke på reduksjon av strømningsmotstanden, at å øke luftspalten er en effektiv tilnærming, som fungerer best innenfor luftspaltehøyder fra ca. 0,023 m til 0,048 m i parameterområdet vurdert i dette arbeidet. Videre er bruk av avrundede steinlekter i luftede tak en annen effektiv måte for å redusere luftstrømningsfriksjonen, eller med andre ord, for å øke strømningshastigheten under de samme strømningsforholdene. Overraskende nok fører en liten avrunding (r = 0,004 m) til en betydelig reduksjon av strømningsfriksjonen (ca. 20%). Derfor antyder dette funnet at den litt avrundede steinlekten, som er relativt enkel å produsere sammenlignet med den mest rundkantete varianten (r = 0,012 m), kan være tilstrekkelig i praktisk bruk av luftede skrå tretak.

Contents

Figure

Table

1 Introduction

1.1 Background

In Norway, wood has been the dominant building material because locally it is easy to access to high-quality raw materials. According to Edvarsen and Ramstad (2006), about 75-80% of new houses were built with wooden frames and the proportion of wooden houses in detached houses is more than 98%. Commercial and service buildings are also often constructed in wood. In addition, the extensive use of wood for exterior and interior cladding is very common. Therefore, the wooden frame structure is an important part of Norwegian building culture and contributes greatly to shaping their environment. Norway's long tradition of the wooden building has shown how architecture and structure technology have developed over several hundred years, which also demonstrates that wood is a solid, flexible, environmentally friendly, and accessible building resource as shown in figure 1.1.

Moreover, the development of the wooden structure building technology is based on and adapting to the local climatic conditions in Norway. Norway is one of the world's most northerly countries with an extremely long coastline and wide mountains, which contribute to a greatly varied climate and seasonal variations. Climate and weather influence most Norwegian’s daily lives, so it is important to take into account the weather and to adapt to the varying climate over the centuries. However, the world’s climate change leads to an increase in average annual precipitation and increased frequency and intensity of heavy rainfall in Norway (Norwegian Ministry of Climate and Environment, 2015). Therefore, today's buildings have to be able to withstand the pressure of the weather and adapt to climate change.

While wood-frame construction is a common building technique in Norway, it is still a challenge to improve the durability of the wood frame structures because wood is susceptible to moisture. Protection of wooden buildings from moisture is an important design criterion, as important as protection from fire or structural collapse. Roof as one of the main building envelopes is the building's most important protection against precipitation. In Norway, it is traditionally preferred to build detached houses and other types of residential small houses with pitched roofs, because sloping roofs are well suited for the climate with heavy rainfalls. However, the increasing volume of rain-induced by climate change causes additional issues on roof structures. In the study by Gullbrekken et al. (2016), they concluded that moisture is the main factor of wooden building defects, especially in the roof constructions. In pitched wooden roofs, about 67% of defects are caused by precipitation or indoor moisture. As well as in connection with the ventilation of the roofing and poorly insulated roof construction.

In this thesis, we explore the pitched roof structures with a focus on the airflow behavior and temperature distribution inside the structures. One main reason that motivates this study is that it is typical in Norway to design the pitched wooden roofs with air-ventilated cavities, as shown in figure 1.2. The purpose of the air-ventilated cavity of such roofs is to remove the building moisture and the moisture that can penetrate the roof structure

through air leaks from the inside building. In addition, snowmelt and subsequent icing at the eaves and gutters are prevented by ventilating the roof sufficiently.

(a) (b)

Figure 1.1: (a) Traditional Norwegian house in Sverresborg Trondelag Folk Museum in Trondheim; (b) Modern Norwegian house (www.dezeen.com).

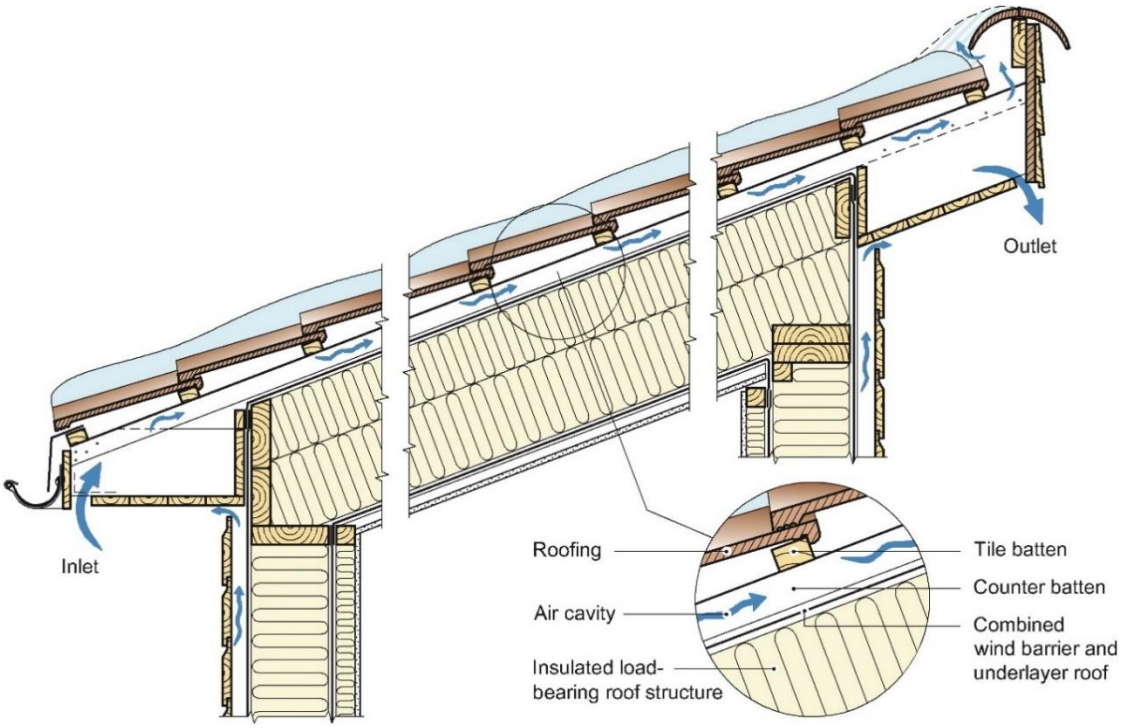

Figure 1.2: Structure of ventilated pitch wooden roof. (Figure by Gullbrekken, 2018).

1.2 Motivation and Objectives

This master thesis is following the work by Eggen & Røer (2018) and to provide a detailed numerical study for the ventilated pitched wooden roofs. This study aims to advance our understanding of the flow physics of airflow in the pitched wooden roofs by means of the Computational Fluid Dynamics (CFD) technique.

The airflow passing through the ventilation layer of the roofs is a complicated flow phenomenon, because various factors have to be considered, such as natural convection induced by the temperature difference of insulation surface and roofing, the pitch angle of the roof, the effect of tile battens, inflow velocity, turbulence, etc. In order to have a deep understanding of the flow phenomenon of the air cavity of pitched wooden roofs, this thesis aims to explore the effects of natural convection, the pitch angle of the roof and the presence of tile battens on the airflow by means of CFD simulations. The focus will be on the analysis of flow behavior and friction loss in different flow configurations. The objectives of the thesis work are to develop a numerical approach for studying the ventilated pitched roofs and to advance the understanding of the flow physics of airflow in the pitched roofs.

The main goal of this master thesis is to clarify how the height of the air cavity and tile battens under the roofing affects the airflow in the cavity. The numerical results from this work will provide useful knowledge for developing new guidelines for ventilated wooden roofs with a pitch angle. The numerical simulations are carried out following the parameters and conditions of laboratory experiments of a physical model developed in the laboratory of NTNU and SINTEF Byggforsk. The numerical results will be compared with the experimental measurements as a validation of the numerical approach.

By means of CFD simulations, I will focus on the flow resistance, which is caused by the airflow passing through a channel with tile battens under the roofing. More specifically, I am interested to investigate the following research questions:

- How is airflow behavior affected by the natural convection induced by the temperature difference of insulation surface and roofing?
- What is the relationship between natural convection and the pitch angle of the roof?
- How is the flow resistance modulated by the presence of tile battens? Will the shape of tile batten play a role in the reduction of flow resistance? If so, what is the optimum shape of the round-edged tile batten?
- How does the air-cavity height influence the local loss coefficient? What is the suitable height of the air cavity for minimizing the flow friction?

Motivated by those important and not fully understood questions, I carry out a series of CFD simulations of different flow configurations.

It should be noted that the present work only focus on the airflow passing through the middle section of the roof, which is not a full-scale simulation of the whole roof. The full-scale simulation could provide a more complete picture of the airflow behavior in the roof. But the difficulties are (1) the huge computation cost and (2) mesh generation for the complicated geometry. Because of the time constraint of the master thesis work, I will only investigate flow in the middle section and the full-scale CFD simulations of the roof are

subject of the future investigation. Another point that I need to clarify is that the numerical approach used in the present work is turbulence-model dependent and to obtain high resolution numerical results an alternative is using more expensive numerical approach, for instance Large-Eddy Simulation, which, of course, needs much more computation resources that cannot be afforded in this thesis work.

The structure of the thesis is organized as follows. Chapter 2 is on the methodology. After a detailed introduction of the background of the roofing in the building construction and relevant knowledge of fluid mechanics and heat transfer, I also briefly descript the numerical method and turbulence modelling that are used in current CFD simulations. All results are collected in Chapter 3, in which I examined the planar channel flow with smooth walls and also the channel flow with different types of tile battens. Some numerical results are in good agreement with the theory and experimental data. The numerical findings are analyzed and discussed, and finally, the conclusions are drawn in Chapter 4 followed by a brief description of the future work in this field.

2 Theoretical Framework

The focus of this work is to advance our understanding of the air flowing in the ventilated air cavity in pitched wooden roofs. How the airflow behaves in the air cavity is a complicated flow phenomenon, which is related not only to the knowledge of roof structure design but also the knowledge of fluid mechanics and heat transfer. The present Chapter will cover the relevant basic concepts of ventilated pitched wooden roofs, theory and governing equations that describe how the air flows inside the pitched roof. The continuity, momentum and energy conservation equations will be briefly introduced, and important physical dimensionless parameters will be defined. Furthermore, this thesis work greatly relies on the numerical study and, therefore, I will also present some details of numerical simulations, including the numerical schemes for the solver and turbulence modellings.

2.1 Ventilated Pitched Wooden Roofs

2.1.1 Principles of pitched wooden roof constructions

The choice of construction principle for ventilation and insulation of the roof structure is of great importance for the roof performance, how the moisture impact is controlled and which materials should be used (Edvarsen & Ramstad, 2006). The main principles are given in figure 2, in which a distinction is made between roofs with cold attic, roofs with partially insulated attic and roofs with full insulation. Regardless of the types of the attic, all roofs with exterior drain pipes have to be ventilated in order to carry away any moisture that escapes up through joints in the insulation and to remove heat transferred through the insulated roof structure to avoid snow melting and forming ice dams at the eaves and gutters (Gullbrekken, 2018).

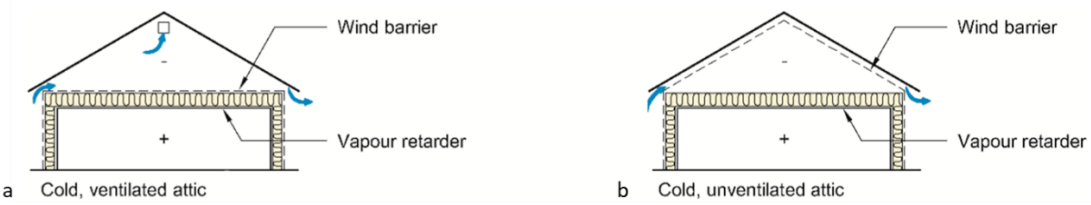

Figure 2.1: Roof with cold attic. (a) Cold, ventilated attic space with air stream flowing through the attic itself. (b) Cold, unventilated attic space with all ventilation between the underlayer roof and the roof covering (Gullbrekken, 2018).

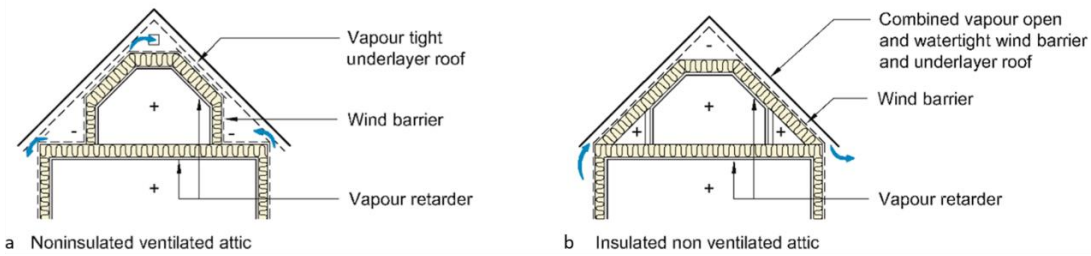

Figure 2.2: Roof with heated rooms in part of the attic. (a) Thermally insulated non-ventilated attic rooms. (b) Thermally non-insulated, ventilated (from outside) attic rooms (Gullbrekken, 2018).

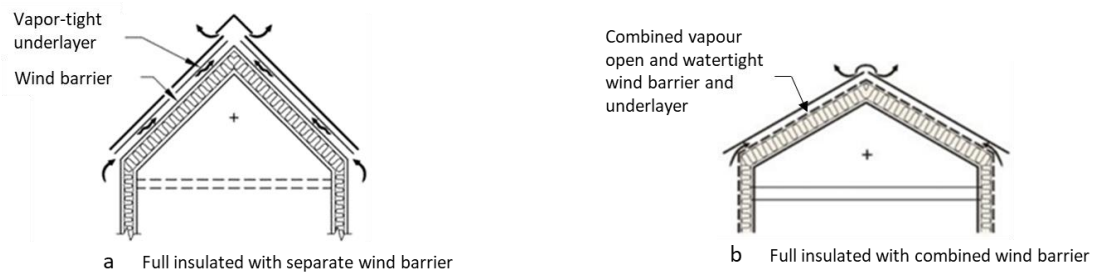

Figure 2.3: Roof with full insulation. (a) A roof separates the rain and wind barrier. (b) An insulated roof with vapor opens combined wind barrier and underlayer roof. All ventilation of the roof takes place in the air cavity below the roofing. (Gullbrekken, 2018).

This master thesis only focuses on the structure of ventilated pitched wooden roof with a combined wind barrier and underlayer roof, as given in Figure 1.2 and Figure 2.3b. According to the research of Gullbrekken (2018), the roof structure built with air cavity is considered robust following the requirements of Roels and Langmans (2016), Edvardsen and Ramstad (2006) and Uvsløkk (1996). Compared to the traditional ventilated pitched wooden roof with separate wind barrier and underlayer roofing, the roof structure with combined wind barrier and underlayer roofing is less material consuming and more labor-efficient. From the outer part, cold side of the structure, this "modern more common" roof structure consists of:

- Rain-tight roofing
- Drainage and ventilation cavity
- Combined vapor open and watertight wind barrier and underlayer roof

The air-ventilated cavity has so far served two purposes:

- Remove excessive moisture from the roof structure including built-in moisture, condensation or any air leaks through the roof structure, which is necessary to avoid mold growth and rot.

- Ventilate heat from the roof structure so that the above temperature in the air cavity is kept as low as possible, with the intention of preventing snowmelt and subsequent ice formation at the eaves and gutters.

According to the study by Gullbrekken (2018), the wood moisture redistribution in the air cavity is caused by natural convection. Natural convection could drive the air to circulate in the cavity, rising on the warm side and dropping on the cold side. The amount of natural

convection depends on the following driving forces and airflow resistance of the insulated cavities:

- Temperature difference across the wall
- Equivalent air permeability of the insulated cavity
- Insulation thickness

Nora et al. (2020) found that the air flow through the air cavity is driven by wind pressure and thermal buoyancy and affected by various factors. Nora (2019) has mentioned that the resulting airflow depends on the dimensions of air cavity, design of the raft and ridge, and flow resistors in the cavity. An efficient way to enhance the ventilation beneath the roofing is the proper design of the counter- and tile battens. Increased counter batten height as well as use of round-edged tile battens are found to reduce the friction loss inside the air cavity. In addition, local wind and temperature conditions are of importance for the air exchange rate in the column. Therefore, the design of air cavity in the roof construction should be adjusted in accordance with the requirements where the house is constructed. In cold and temperate climates, for instance the Nordic countries, ventilation of attics or roofs is essential.

2.1.2 Norwegian guidelines of air cavity design

The guidelines for the design of air cavity in pitched wooden roofs in Norway are presented in SINTEF Building Design Guides (Byggforskserien), which are based on the previous research work within the field. However, the air cavity design of roofs with larger roof spans and lower angles is insufficient (Gullbrekken, 2018). Existing air cavity design guidelines for Norway state a maximum roof length from eaves to ridge of 15 m and a minimum roof pitch 10 to 15 degrees. For roofs with separated wind barrier and underlayer roofing, the guidelines of Bøhlerengen (2007) include detailed specifications of air cavity design for roof length up to 7 m and roof angle lager than 10 to 15 degrees. In the meanwhile, for the roofs with combined underlayer roof and wind barrier (watertight vapour-open membrane), the guidelines of Bøhlerengen (2012) include the details for roof length up to 15 m and roof angle larger than 18 to 22 degrees. The guidelines for pitched wooden roofs with combined wind barrier and underlayer roofing are given in Table 1.

It shows that there is no recommendations are given for roofs with larger dimensions and lower angles than those described in Table 1. The lack of guidelines is one reason for preferring compact roofs (Gullbrekken, 2018). To develop new guidelines for including a wider range of ventilated pitched roof constructions, it is essential to have a comprehensive understanding of the operation of the air cavity. The theory that describes the physics of airflow in the air cavity is presented in the following sections.

Table 1 Recommended loop height (mm) depending on the angle and length of the roof. (Byggforskserien 525.102)

Roof angle	Roof length (m)		
	7,5	10	15
18-30 °	36	36 + 36	48 + 48
31-40 °	30	36	36 + 23
≥ 41 °	23	36	36 + 23

2.2 Theory and Governing Equations of Airflow

2.2.1 Basic phyiscal quantities of airflow

Generally, the Newtonian fluid flow with a constant viscosity can be divided into two groups, i. e. *incompressible* flow and *compressible* flow. The incompressible flow refers to the fluid flow with a constant density ρ and the compressible flow undergoes a variation of fluid density ρ. The fluid considered in present work is air, which is Newtonian and can be either compressible or incompressible depending on the flow speed. The air is becoming compressible when the value of Mach number crosses above 0.3. Here, the Mach number is the ratio between flow speed and the speed of sound. Considering the air flow in a pitched roof, the flow speed is much smaller than the speed of sound, which leads to a value of Mach number greatly less than 0.3. Therefore, in the present work, the airflow is Newtonian and incompressible.

The *density of air* ρ can be defined as the mass of air ΔM divided the air volume $\Delta\tau$ as,

$$\rho = \lim_{\Delta\tau \to 0} \frac{\Delta M}{\Delta \tau} \tag{1}$$

Here, the air density is dependent on temperature and pressure, and the density gradually reduces with increasing the temperature. At one atmosphere pressure, the air density is about 1.225 kg/m^3 at 15 °C.

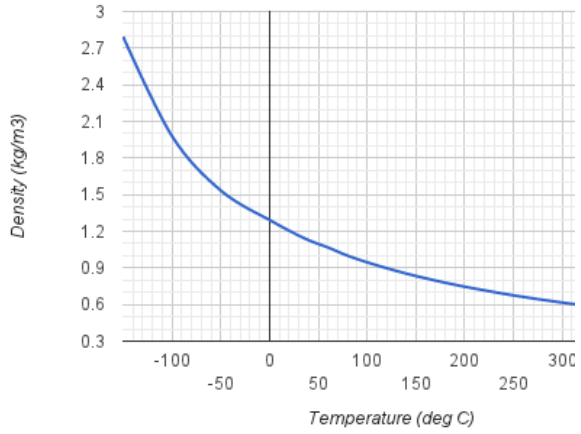

Figure 2.4: Air density versus temperature at one atmosphere pressure.

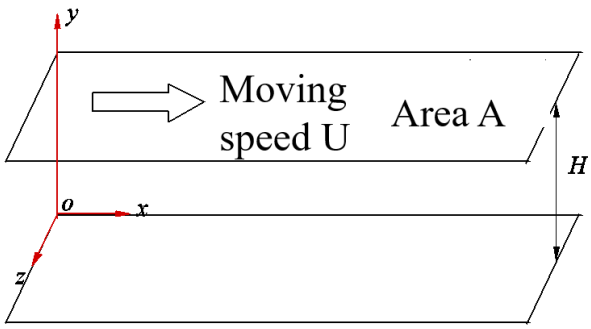

Figure 2.5: A sketch of planar Couette flow with a moving upper plane.

Another important physical parameter of airflow is *viscosity*, which is a measure of fluid resistance to deformation at a given shear rate and is essentially an outcome of air molecular interactions. The viscosity can be measured by a planar Couette flow as shown in figure 2.2 and the derivation of the dynamic viscosity μ is given in Equation (2).

$$\frac{F}{A} \propto \frac{U}{H}, \qquad \tau \equiv \frac{F}{A} = \mu \frac{U}{H}, \qquad \tau = \mu \frac{\mathrm{d}U}{\mathrm{d}y}, \tag{2}$$

Here, the shear stress τ is linearly proportional to the gradient of velocity U [ms^{-1}] and the coefficient μ is defined as the *dynamic viscosity* with a dimension as [$Nm^{-2}s$]. Furthermore, the viscosity can be expressed in another way as the *kinematic viscosity* ν [m^2s^{-1}],

$$\nu = \frac{\mu}{\rho}. \tag{3}$$

The viscosity of air greatly depends on the temperature and figure 2.3 shows the variation of dynamic viscosity with increasing temperature. The dynamic viscosity of air at 15 °C is about 1.81×10^{-5} [Nsm^{-2}] at one atmosphere pressure.

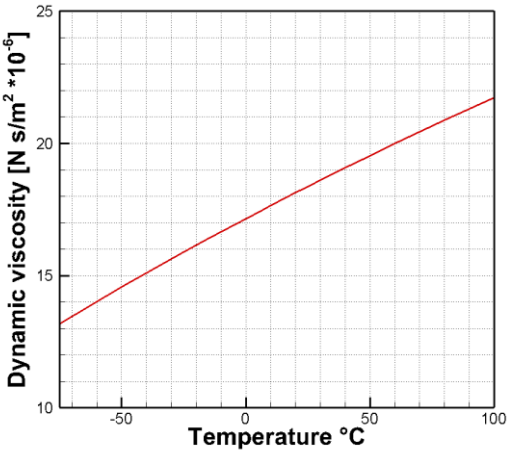

Figure 2.6: Air dynamic viscosity versus temperature at one atmosphere pressure.

2.2.2 Conservation equations

Basically, due to incompressibility the momentum equation is decoupled with energy equation and the governing equations are therefore simplified compared with the equations of compressible case. For the incompressible Newtonian fluid flow, the governing equations are continuity equation, momentum conservation equation (Naiver-Stokes equation) and energy conservation equation:

$$\nabla \cdot \mathbf{V} = 0\,, \tag{4}$$

$$\frac{\partial \mathbf{V}}{\partial t} + \mathbf{V} \cdot \nabla \mathbf{V} = \mathbf{f} - \frac{1}{\rho}\nabla p + \nu \nabla^2 \mathbf{V}\,, \tag{5}$$

$$\frac{\partial}{\partial t}(e + \tfrac{1}{2}|\mathbf{V}|^2) + \mathbf{V} \cdot \nabla(e + \tfrac{1}{2}|\mathbf{V}|^2) = \mathbf{f} \cdot \mathbf{V} + \frac{1}{\rho}\nabla \cdot (\mathbf{T} \cdot \mathbf{V}) + Q + \frac{1}{\rho}\nabla \cdot (\lambda \nabla \theta)\,, \tag{6}$$

where $\mathbf{V}$ is the fluid velocity vector, ∇ is the Nabla operator, the symbol $\cdot$ stands for the vector product, $\mathbf{f}$ represents the external force vector, p is the instantaneous pressure. In equation 6, i.e. the energy equation, e is the internal energy, $\mathbf{T}$ is the stress tensor, Q is the external energy input, λ is the thermal conductivity coefficient, and θ is the temperature. The stress tensor $\mathbf{T}$ for incompressible Newtonian flow can be expressed as

$$T_{ij} = -p\delta_{ij} + 2\mu S_{ij}\,, \tag{7}$$

$$\frac{\partial V_j}{\partial x_i} = \frac{1}{2}\left(\frac{\partial V_j}{\partial x_i} + \frac{\partial V_i}{\partial x_j}\right) + \frac{1}{2}\left(\frac{\partial V_j}{\partial x_i} - \frac{\partial V_i}{\partial x_j}\right) = S_{ij} + \Omega_{ij}\,. \tag{8}$$

Here, the stress tensor T_{ij} is represented by using the strain tensor S_{ij} defined in equation (8). The subscript i or j stands for the i or j component. The velocity gradient tensor can be decomposed into two parts as shown in equation (8), i. e. the strain tensor S_{ij} and the rotation tensor Ω_{ij}.

The Kronecker delta, δ_{ij} , is defined as:

$$\delta_{ij} = \begin{cases} 1 & i = j \\ 0 & i \neq j \end{cases}, \tag{9}$$

Note that hereinafter the notations of vector and tensor are written using bold fonts to differ with the scalars.

2.2.3 Non-dimensionalization and dimensionless parameters

The conservations equations can be normalized for better analyzing the dominance of each term. For the non-dimensionalization process, first, we can choose characteristic flow scales, including time scale T, length scale L, velocity scale V, gravity acceleration g, and

reference pressure *p*. Using these characteristic scales, the momentum equation (5) can be written as:

$$\left(\frac{L}{VT}\right)\frac{\partial u_i^*}{\partial t^*}+u_j^*\frac{\partial u_i^*}{\partial x_j^*}=\left(\frac{gL}{V^2}\right)f_i^*-\left(\frac{P}{\rho V^2}\right)\frac{\partial p^*}{\partial x_i^*}+\left(\frac{\nu}{VL}\right)\frac{\partial^2 u_i^*}{\partial x_j^*\partial x_j^*}, \tag{10}$$

where the superscript * represents the dimensionless quantity. Each coefficient in the parentheses stands for a different non-dimensional parameter, which has its own physical meaning.

$$St\equiv\frac{L}{VT}, \tag{11}$$

$$Fr\equiv\frac{V^2}{gL}, \tag{12}$$

$$Eu\equiv\frac{P}{\rho V^2}, \tag{13}$$

$$Re\equiv\frac{VL}{\nu}, \tag{14}$$

Strouhal number *St* represents a measure of the dominance of the unsteadiness of the flow, for instance, if the St is small the flow can be assumed to be a steady flow. The Froude number *Fr* defined as the ratio of the flow inertial force to the external force (gravity force). The Euler Number *Eu* can be interpreted as a measure of the ratio of the pressure force to the fluid inertial force. Lastly, as one of the most important dimensionless parameters in fluid mechanics, the Reynolds number *Re* is expressed as the ratio of fluid inertial force to the viscous force. The Reynolds number is named after Osborne Reynolds (1883), who conducted the first experiment of pipe flow to demonstrate the two distinct flow regimes, i.e. laminar and turbulence. Therefore, the Reynolds number can be widely used to categorize the fluids patterns in different flow configurations, in which the effect of viscosity and the effect of fluid inertia can be compared by using the Reynolds number. Generally, the flows are laminar at low Reynolds numbers while the flows tend to be turbulent at high Reynolds number. In a pipe flow, laminar flow occurs when Re < 2300 and turbulent flow is fully developed at Re > 2900. Between the two Reynolds numbers, the flow is in the transition state.

The present work is exploring the flow in a pitched roof and the flow configuration is similar to the *planar channel flow* (also called as *Poiseuille flow*), in which the flow is passing through two parallel solid walls. Flow can be driven by either nature convection or outside wind pressure gradient. In practice, when the Reynolds number is larger than around 3000, the channel flow is in the regime of turbulence. While laminar channel flow is normally with Reynolds number smaller than about 2000. In the following subsection, we will introduce the flow characteristics of laminar channel flow and turbulent channel flow.

2.2.4 Laminar channel flow

Laminar channel flow is one of the steady parallel flows and the velocity components in the spanwise direction and wall-normal direction are zero. The only non-zero streamwise velocity is time-independent and only varies in the wall-normal direction and the near-wall velocity gradient induces the wall shear stress, which results in the wall friction and pressure loss. In the following we will derive the theoretical wall friction factor of laminar channel flow, which will be used to validate our numerical simulation in the Section of Results.

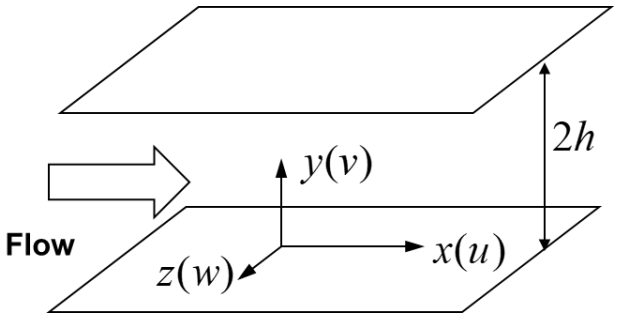

Figure 2.7: A sketch of channel flow.

The three velocity components in the streamwise, wall-normal and spanwise direction in a laminar channel flow are given as,

$$U = f(y), \quad V = 0, \quad W = 0 \tag{15}$$

The Navier-Stokes equation (5) then can be written as

$$\frac{dp}{dx} = \mu \frac{\partial^2 U}{\partial y^2} \tag{16}$$

The boundary condition is: $U = 0$ at $y = \pm h$ and due to the zero pressure gradient in the spanwise direction $\partial p / \partial y = 0$ the pressure in the streamwise direction is then constant as $\mathrm{d}p/\mathrm{d}x = const.$ Therefore, the streamwise velocity U can be obtained as,

$$U = -\frac{1}{2\mu}\frac{\mathrm{d}p}{\mathrm{d}x}\left(h^2 - y^2\right) \tag{17}$$

Here we can see that the maximum streamwise velocity is located at the centerline as,

$$U_c = \frac{h^2}{2\mu}\left(-\frac{\mathrm{d}p}{\mathrm{d}x}\right) \tag{18}$$

The bulk velocity is $U_b = 2U_c/3$ and expressed as,

$$U_b = \frac{h^2}{3\mu}\left(-\frac{dp}{dx}\right) \tag{19}$$

Furthermore, we can obtain the shear stress as,

$$\tau_{xy} = -\frac{\mathrm{d}p}{\mathrm{d}x}y, \tag{20}$$

The wall shear stress $\tau_w = h\mathrm{d}p/\mathrm{d}x$ at the wall $y = h$. The friction factor λ is defined as the wall stress normalized by the dynamic pressure $\frac{1}{2}\rho U_b^2$. Then by using equation (19) the friction factor can be written as,

$$C_f = \frac{\tau_w}{1/2\rho U_b^2} = -\frac{h}{1/2\rho U_b^2}\frac{\mathrm{d}p}{\mathrm{d}x} = \frac{\mu}{\rho U_b h}\frac{h^2}{1/2\mu}\frac{\mathrm{d}p}{\mathrm{d}x}\frac{3\mu}{h^2}\frac{\mathrm{d}x}{\mathrm{d}p} = \frac{12}{\mathrm{Re}} \tag{21}$$

Therefore, the friction factor of laminar channel flow is only Reynolds number dependent. Here the Reynolds number Re is defined as $\mathrm{Re} = \rho U_b 2h/\mu$. Note that friction factor of circular pipe laminar flow is $64/\mathrm{Re}$.

2.2.5 Turbulent channel flow

At Reynolds number higher than about 3000, the channel flow becomes turbulent. Different from laminar flow, the motion of turbulent flow undergoes irregular fluctuation, which means the direct and magnitude of fluid velocity continuously varying in both time and space. Because of the chaotic characteristics of turbulent flows, there is so far no exact definition of turbulence yet but the common features of turbulent flow have been summarized by earlier studies (Pope book) including irregularity, dissipation, diffusivity, vorticity, multi-scale, coherent structure, etc. Turbulence is not a fluid property, but a state of the fluid.

(a)

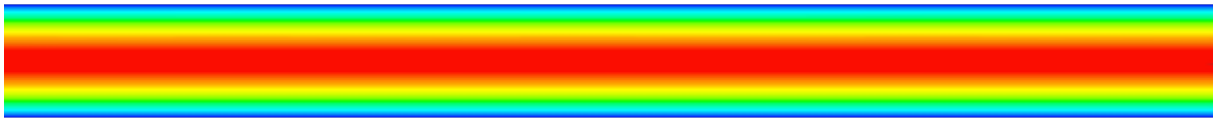

(b)

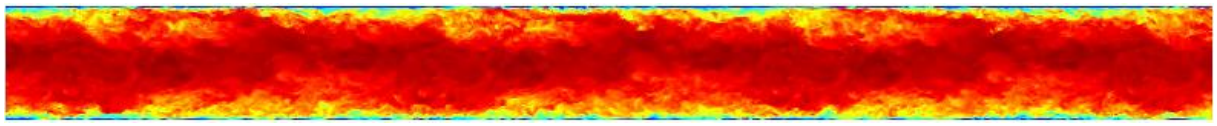

Figure 2.8: Flow contour of the streamwise velocity (a) laminar channel flow and (b) turbulent channel flow (Kim et al. 1987).

The aforementioned features of the turbulent flow make this type of flow more complicated than laminar flow and there is no theoretical solution available for the turbulent channel flow. However, this type of flow can be studied by different numerical approaches, which is the tool that the present thesis work relies on and will be introduced in a later section. Here, in the following we will briefly introduce the mean flow characteristics of turbulent channel flow by only the theoretical analysis.

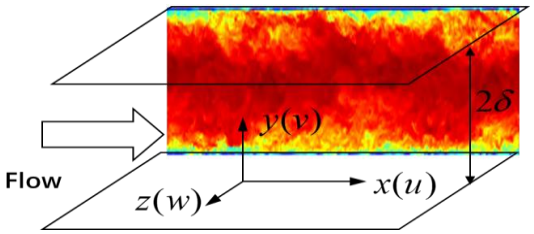

Figure 2.9: A sketch of turbulent channel flow.

In the analysis of turbulent flow, an instantaneous quantity can be decomposed into a mean term expressed by using the symbol $\langle\ \rangle$ and a fluctuation term expressed with a prime $'$, which is the so-called *Reynolds decomposition*. Because in a statistical point of view the turbulent channel flow is steady, $\partial\langle\ \rangle/\partial t = 0$, and homogenous in the streamwise and spanwise directions. The mean velocity in the streamwise, spanwise and wall-normal directions of the channel flow are therefore given as,

$$\langle u\rangle = U(y), \quad \langle v\rangle = 0, \quad \langle w\rangle = 0 \tag{22}$$

The fluctuation velocities are zero after averaging as,

$$\langle u'\rangle = \langle v'\rangle = \langle w'\rangle = \langle v'w'\rangle = \langle u'w'\rangle = 0 \tag{23}$$

Accordingly, the momentum equation in the streamwise, spanwise and wall-normal direction are written as:

$$0 = -\frac{1}{\rho}\frac{\partial\langle p\rangle}{\partial x} + \nu\frac{\partial^2 U}{\partial y^2} - \frac{\partial}{\partial y}\langle u'v'\rangle \tag{24}$$

$$0 = -\frac{1}{\rho}\frac{\partial\langle p\rangle}{\partial y} - \frac{\partial}{\partial y}\langle v'^2\rangle \tag{25}$$

$$0 = -\frac{1}{\rho}\frac{\partial\langle p\rangle}{\partial z} \quad . \tag{26}$$

By integrating the equation (25) and then replace the pressure gradient term in equation (25), we can obtain,

$$\frac{1}{\rho}\frac{\mathrm{d}p_w}{\mathrm{d}x} = \nu\frac{\partial^2 U}{\partial y^2} - \frac{\partial}{\partial y}\left\langle u'v'\right\rangle \quad . \tag{27}$$

Here p_w is the pressure at the wall and *v* is the kinematic viscosity. By integrating equation (27) from 0 to y, we obtain the stress balance equation of turbulent channel flow as:

$$\mu\frac{\partial U}{\partial y} - \rho\left\langle u'v'\right\rangle = \tau_w\left(1-\frac{y}{\delta}\right). \tag{28}$$

Here τ_w is the wall shear stress and μ is the dynamic viscosity. The equation (28) represents the balance of the three stress terms, i.e. viscous stress $\mu\partial U/\partial y$, turbulence stress $-\rho\left\langle u'v'\right\rangle$, total stress $\tau_w\left(1-y/\delta\right)$, in turbulent channel flow. Note that the term of turbulence stress cannot be obtained because the Reynolds-averaged mass conservation equation and Navier-Stokes equation are not closed. Therefore, the turbulence stress has to be modelled in Reynolds-averaged Navier-Stokes (RANS) simulation.

Considering the importance of wall friction, the curve of friction factor versus Reynolds number of channel flow is shown in figure 2.7. The symbols are measurement data from different experiments of smooth and rough pipe flows (Moody 1944). The experimental data at low Reynolds number shows that the friction factor is linearly dependent on the Reynolds number, which is consistent with the earlier theoretical analysis $C_f = 64/\mathrm{Re}$. The curve of friction factor of turbulent flow regime is flatter and the reduction of friction factor is less with increasing Reynolds number compared with laminar case. In addition, the roughness of the wall plays an important role in the friction factor.

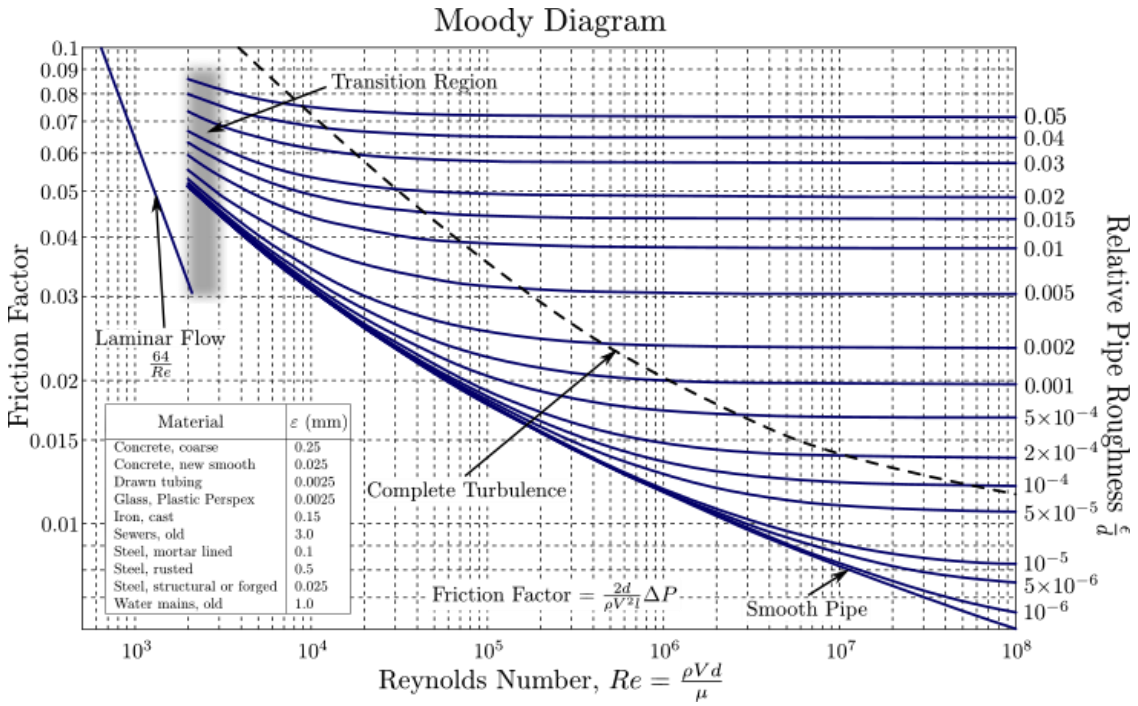

Figure 2.10: A sketch of turbulent channel flow (Moody 1944).

2.2.6 Channel flow with riblet roughness on one side

The air flow passing through a roof with tile battens as shown in figure 2.8 is essentially identical to a channel flow with riblet-like roughness (see figure 2.9), which has been widely studied in past decades (ref…).

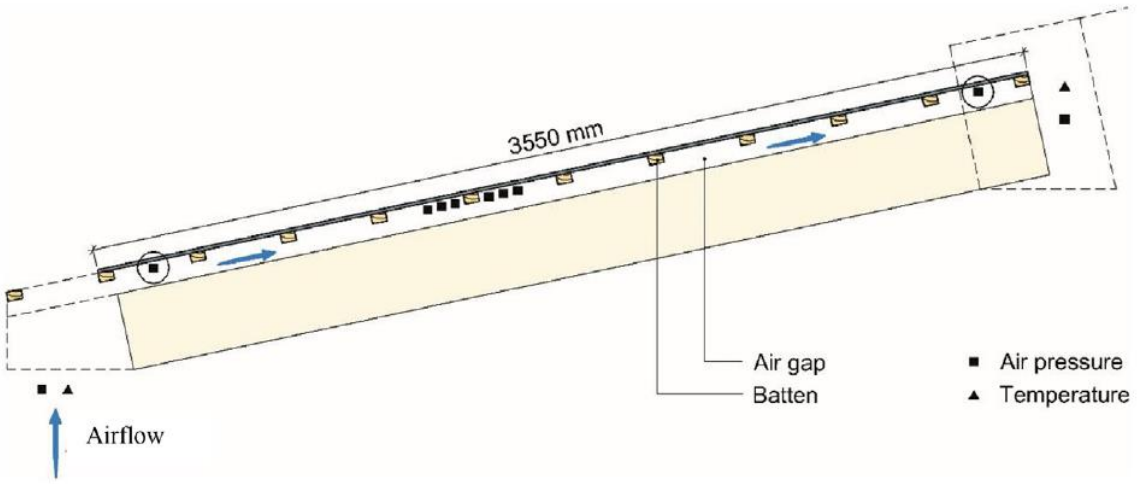

Figure 2.11: A sketch of roof with tile battens (Gullbrekken et al. 2017).

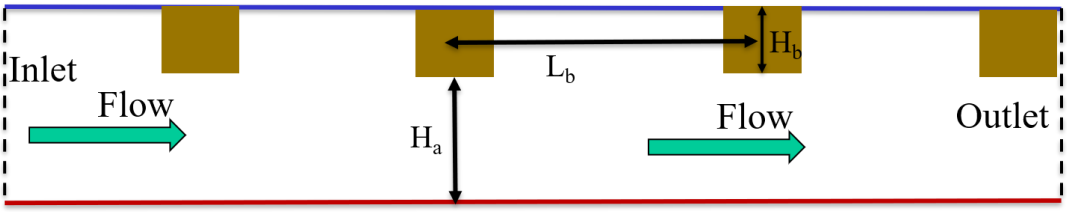

Figure 2.12: A sketch of a channel flow with transverse rib-roughness elements on the upper side.

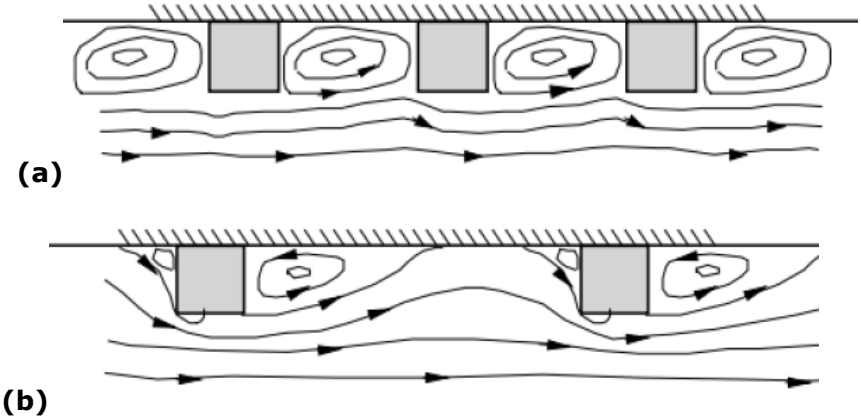

Figure 2.13: A sketch of two types of typical roughness (a) d-type, (b) k-type (figure from Ashrafian et al. 2004).

In practice, there are infinite types of roughness but in the present study we are particularly interested in one type of 2D roughness, which is the spanwise rectangular ribs attached on the upper walls (shown in figure 2.9) as a simplified model of a roof with tile battens. Several geometrical parameters can be used to describe the characteristics of the ribs as the center-to-center distance of two ribs (or battens) L_b, the height of ribs H_b and the distance from lower wall to the battens' surface H_a. Based on the ratio between L_b and H_b, i.e. so-called pitch-to-height ratio λ, this 2D roughness model has two types of rib-roughness as shown in figure 2.10. One is called d-type, in which Lb / Hb ≤ 2 ((e.g. Perry et al., 1969; Wood and Antonia, 1975; Djenidi et al., 1999)). The other one is called k-type, which has larger battens spacing and Lb / Hb > 4 (Raupach 1992, Raupach et al. 1993). The flow passing these two types of rib-roughness are distinctly different as shown in the sketch of flow pattern in figure 2.10. In the case of d-type, stable vortices are formed in the cavities. However, the k-type flow configuration leads to the formation of asymmetric vortices in front and behind the rib element and the reattachment points of the vortices are dependent on the flow Reynolds number.

Regarding the effect of roughness, earlier studies found that friction is greatly dependent on the pitch-to-height ratio λ. As pointed by Leonardi et al. (2003, 2007) and Furuya et al. (1976), the maximum form drag and total friction occur at $\lambda = 7$ but at $\lambda > 7$, the recirculation zones occur in upstream and downstream of each rib but the streamlines and the skin frictional drag reveal that each rib is isolated, which means the ribs do not affect each other. In the case of a pitched roof, the corresponding pitch-to-height ratio is about 7 to 11 (Gullbrekken et al. 2017), therefore we can expect the reduction of friction with increasing of pitch-to-height ratio according to earlier studies. The detailed results will be discussed in the Section of Results.

Furthermore, in our case the height of the roughness is ranging from about 40% to 50% of the channel height and roughness element can be also considered as an obstacle or a bluff body attached on the solid wall. Therefore, the validation of earlier conclusions made for the roughness with relatively small height has to be checked in the present study.

2.2.7 Natural convection between two solid walls

Another important factor to be considered in the present thesis is the natural convection induced by the temperature difference between the upper and lower surface of ventilated roof. The driving force of flow motion of natural convection is the buoyancy, which is dependent on the fluid density. Temperature gradient could result in density difference, which affects the buoyancy and thus cool air falls and warm air rises. One of the key features of natural convection is enhancing heat transfer because of the convective motion of fluid flow. This feature has been used in different industrial applications of cool systems. In contrast to the examples of cooling system, in the present study of ventilated roof, the design normally aims to attenuate such natural convection effect to reduce the heat transfer from the surface of insulation to the roofing, which can keep the low temperature of roofing and avoid snow melting. The sketch of buoyancy-driven natural convection is given in figure 2.11.

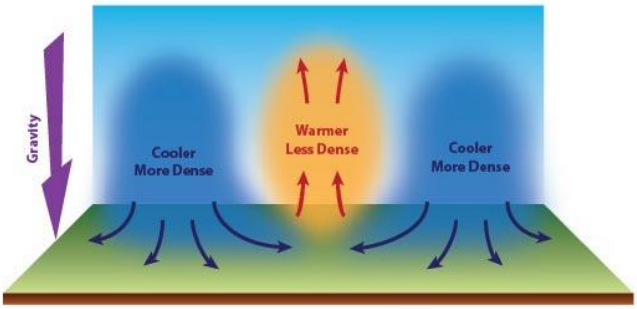

Figure 2.14: A sketch of buoyancy-driven natural convection (figure: www.boydcorp.com).

The natural convection in the ventilated roof can be simplified as the convective flow between two solid walls with different temperatures. According to Oberbeck (1879) - Boussinesq (1903) approximation, the fluid density ρ is assumed to depend linearly on the temperature θ, the non-dimensionlized governing equations are given as

$$\frac{\partial \theta}{\partial t} + \mathbf{u} \cdot \nabla \theta = \Delta \theta \,, \tag{29}$$

$$\frac{1}{\mathrm{Pr}}\left(\frac{\partial \mathbf{u}}{\partial t} + \mathbf{u} \cdot \nabla \mathbf{u}\right) - \Delta \mathbf{u} + \nabla p = Ra\theta \mathbf{e}_g \,, \tag{30}$$

$$\nabla \cdot \mathbf{u} = 0 \,, \tag{31}$$

where **u** is the velocity vector of fluid and p is the pressure. Δ is the symbol of Laplace operator and $\mathbf{e}_g$ is the vector of gravity direction. There are two dimensionless parameters the Prandtl number, *Pr*, and the Rayleigh number, *Ra*.

By definition the Prandtl number is written as:

$$\mathrm{Pr} = \frac{\upsilon}{\alpha} \tag{32}$$

where υ is the kinematic viscosity and α is the thermal diffusivity, in the case of air, thermal diffusivity is 2×10-5 m2/s at 20°C and atmospheric pressure. Prandtl number is named after the German physicist Ludwig Prandtl, defined as the ratio of momentum diffusivity to thermal diffusivity.

Furthermore, Rayleigh number, *Ra*, is defined as:

$$\mathrm{Ra} = \mathrm{Gr} \cdot \mathrm{Pr}, \tag{33}$$

$$\mathrm{Gr} = \mathrm{Re}^2 \frac{g\beta\Delta\theta L}{\upsilon^2}, \tag{34}$$

where *Gr* is the Grashof number defined as the ratio of the buoyant force to viscous force acting on a fluid element. β is the thermal expansion coefficient and Δθ represents the temperature difference. Thermal expansion coefficient of air changes with its temperature. At the normal standard conditions of 25 °C or 298 Kelvin, the thermal expansion coefficient of air is around 0.0034/K. Therefore, the Rayleigh number, Ra, is rewritten as:

$$\mathrm{Ra} = \frac{g\beta\Delta\theta L^3}{\upsilon\alpha}, \tag{35}$$

Another dimensionless parameter, which measures the effectiveness of convective motion and quantifies the enhancement of vertical heat flux due to convection, is the Nusselt number Nu. Malkus (1954) predicted the scaling law as Nu ~ Ra1/3.

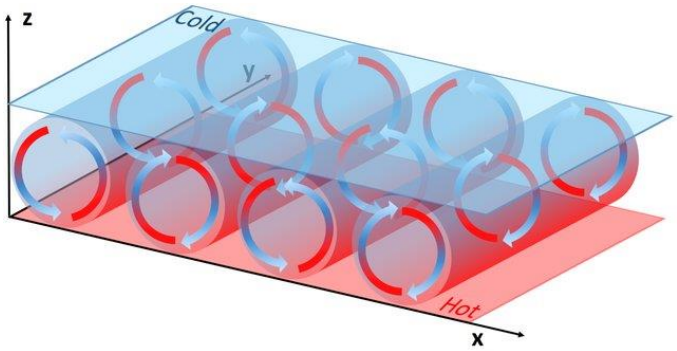

Figure 2.15: A sketch of convection rolls in Rayleigh-Bènard convection (Barna et al. 2017).

Again, note that the natural convection in the ventilated roof with neglecting the inclination is similar to Rayleigh-Bènard convection, which consists two parallel horizontal plates with a distance H. The lower wall has higher temperature than the upper wall, which gives an unstable system. In Rayleigh-Bènard flow configuration, the convection occurs when Ra > 1700 and the flow is laminar or turbulent when Rayleigh number is less 108 or larger than 109, respectively.

2.3 Numerical Approach

Experiment and numerical simulations are the two main approaches for studying the problems of roof ventilation. With the quick development of computing facility, computational fluid dynamics (CFD) simulation has been developed quickly and become more and more popular in the past decades. CFD was firstly used in the field of aerospace research and then was employed in the study of other engineering fields, such as civil engineering and chemical engineering. In general, there are three essential parts included in a standard CFD code or software, which are the pre-processing part, solver part and post-processing part. The first part includes geometry building, meshing, and setting of boundary conditions. The solver part contains numerical methods and models for solving the governing equations of the flow problem. The post-processing part is mainly for flow data visualization and sometimes for averaging samples to obtain the statistics.

In this section, the relevant information about the numerical approach used in the present thesis will be introduced. The numerical simulations will be carried out by using ANSYS Fluent. I will first describe the turbulence modelling and then the solvers that are employed in this commercial Computational Fluid Dynamics (CFD) software.

2.3.1 Turbulence modelling

Turbulence is known as "the last unsolved problem of classical physics" and a key in the understanding of various flow phenomena. The flow passing the ventilated roof can be turbulent when the speed of airflow is relatively high. In general there are basically three approaches for turbulence simulations. The first one *Direct Numerical Simulation* (DNS) is a high-fidelity numerical technique for turbulent flow simulations, solving the full Navier-Stokes equations without any semi-empirical turbulence model. DNS is evolving as one of the most important approaches for turbulence physics research due to the fast development of high-performance computing (HPC). However, the expense of DNS computations is exponentially increasing with the flow Reynolds number and, therefore, the cost of DNS limits its application in practical problems. The second approach is *Large Eddy Simulation* (LES), which is a less computationally expensive method than DNS. LES fully resolves the large-scale fluid motion but uses a subgrid model for the turbulent motion with the scale smaller than the grid resolution. Even though LES is cheaper than DNS but LES is still expensive and not widely used in the engineering application. The last approach is *Reynolds Averaged Navier-Stokes* (RANS) simulation, in which only the averaged fluid motion is computed. The RANS simulation so far is the most popular approach in engineering applications because concerning the engineering needs the mean flow properties are sufficient and on the other hand the efficiency is an essential factor to be considered. Figure 2.13 shows an example of a jet flow contour simulated by the three different approaches. It is obvious that each approach captures different levels of details of the flow. The RANS approach only provides information of mean flow motion.

Considering that there are many parameters to be studied in the current work, there is a series of cases to be computed. To have all simulations done within the time constraint of thesis work, the RANS approach is chosen. As mentioned earlier the RANS equations are not closed, therefore, turbulence model is required for solving the RANS equations. In the following, I will introduce the Reynolds averaging and typical turbulence models.

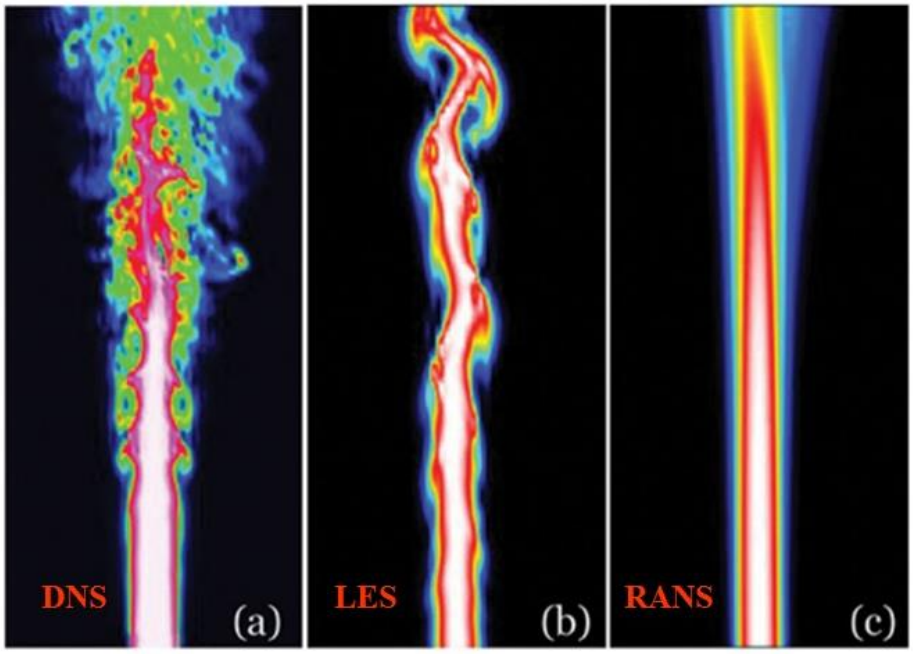

Figure 2.16: Comparison of a DNS (a), LES (b) and RANS (c) simulation of a jet flow (Italian Agency for New Energy Technologies 2006).

First of all, the equation of mean flow will be introduced. The equation (4 - 6) can be averaged by means of Reynolds decomposition that an instantaneous quantity q can be decomposed into the mean and fluctuation term as $q = \langle q \rangle + q'$ and the following rules should follow,

$$\langle \langle q \rangle \rangle = \langle q \rangle,\ \langle q' \rangle = 0,\ \langle \langle f \rangle q' \rangle = 0\ ,\ \langle f + g \rangle = \langle f \rangle + \langle g \rangle\ ,\ \left\langle \frac{\partial f}{\partial t} \right\rangle = \frac{\partial \langle f \rangle}{\partial t}. \tag{36}$$

Following the Reynolds decomposition, we can obtain the RANS-Reynolds-averaged Navier–Stokes equation and mass conservation equation for incompressible Newtonian flow as:

$$\frac{\partial \langle V_i \rangle}{\partial t} + \langle V_j \rangle \frac{\partial \langle V_i \rangle}{\partial x_j} = -\frac{1}{\rho}\frac{\partial \langle p \rangle}{\partial x_i} + \nu \frac{\partial^2 \langle V_i \rangle}{\partial x_j \partial x_j} - \frac{\partial}{\partial x_j}\langle V_i V_j' \rangle, \tag{37}$$

$$\frac{\partial \langle V_i \rangle}{\partial x_i} = 0\ . \tag{38}$$

Here, *i* and *j* are the subscripts as *i* = 1, 2, 3 and *j* = 1, 2, 3 to represent the velocity component in *x*, *y*, and *z* direction, respectively. It is obvious that there are 4 equations but 10 unknowns, which means the set of equations is not closed. To solve the RANS equation, we need to model the term of $\langle V_i V_j' \rangle$, which is so-called Reynolds stress or turbulence stress. Using the additional equations to model the unknown Reynolds stress is called turbulence modeling.

In the past decades about more than one hundred turbulent models have been developed for different engineering problems, and generally they can be classified into four classes:

- Zero-equation (Algebraic) turbulence model: Prandtl mixing length model, Cebeci-Smith model, Baldwin-Lomax model, etc.
- One-equation turbulence model: Spalart-Allmaras model, Baldwin-Barth etc.
- Two-equation turbulence model: *k*-ε model, *k*-ω model, and so on.
- Seven-equation turbulence model: Reynolds stress model.

Considering the constraint of space, we will only introduce the most popular model, i.e. *k*-ε model, which is also used in the simulation of the current study. This model needs two equations for solving the turbulent kinetic energy *k* and turbulent dissipation rate ε, which are defined as:

$$k \equiv \tfrac{1}{2}\left\langle V_i' V_i' \right\rangle , \tag{39}$$

$$\varepsilon = \frac{1}{2}\varepsilon_{ii} = \nu \left\langle \left(\frac{\partial V_i'}{\partial x_j} \right)^2 \right\rangle . \tag{40}$$

Note that the Einstein summation convention, which is a way to write vector and tensor expressions in a compact way, is used and the same index appears twice in a term representing a summation over all values of that index, for instance, $k \equiv \tfrac{1}{2}\left\langle V_i' V_i' \right\rangle = \tfrac{1}{2}\left\langle V_1' V_1' + V_2' V_2' + V_3' V_3' \right\rangle$.

According to Boussinesq hypothesis (1877), the Reynolds stress can be written as

$$-\left\langle V_i' V_j' \right\rangle = 2\nu_T \left\langle S_{ij} \right\rangle - \tfrac{2}{3} k\delta_{ij} \ , \tag{41}$$

Here $S_{ij} = \frac{1}{2}\left(\frac{\partial \langle V_i \rangle}{\partial x_j} + \frac{\partial \langle V_j \rangle}{\partial x_i}\right)$ is the mean strain rate of fluid and ν_T is the eddy viscosity coefficient. The Reynolds stress can be obtained if the turbulent kinetic energy *k* and eddy viscosity ν_T are known. Considering the dimension of *k* and ε, we can try to construct the eddy viscosity coefficient ν_T as:

$$l \sim \frac{k^{3/2}}{\varepsilon}, \quad u \sim k^{1/2} \ , \tag{42}$$

$$\nu_T \sim u \cdot l \sim \frac{k^2}{\varepsilon} \ , \tag{43}$$

$$\nu_T = C_\mu \frac{k^2}{\varepsilon} . \tag{44}$$

Here C_μ is a constant coefficient, which needs to be determined by experiment. Note that the eddy viscosity ν_T is artificially created to close the momentum equations but not physical quantity.

Further, the turbulent kinetic energy *k* and turbulent dissipation rate ε can be computed by the following two equations:

$$\frac{\partial k}{\partial t}+\langle V_j\rangle\frac{\partial k}{\partial x_j}=\nu_T\left(\frac{\partial\langle V_i\rangle}{\partial x_j}+\frac{\partial\langle V_j\rangle}{\partial x_i}\right)\frac{\partial\langle V_i\rangle}{\partial x_j}+\frac{\partial}{\partial x_j}\left[\left(\nu+\frac{\nu_T}{\sigma_k}\right)\frac{\partial k}{\partial x_j}\right]-\varepsilon\ , \tag{45}$$

$$\frac{\partial \varepsilon}{\partial t}+\langle V_j\rangle\frac{\partial \varepsilon}{\partial x_j}=C_{\varepsilon 1}\frac{\varepsilon}{k}\nu_T\left(\frac{\partial\langle V_i\rangle}{\partial x_j}+\frac{\partial\langle V_j\rangle}{\partial x_i}\right)\frac{\partial\langle V_i\rangle}{\partial x_j}+\frac{\partial}{\partial x_j}\left[\left(\nu+\frac{\nu_T}{\sigma_\varepsilon}\right)\frac{\partial \varepsilon}{\partial x_j}\right]-C_{\varepsilon 2}\frac{\varepsilon^2}{k}\,. \tag{46}$$

Here σ_k and σ_ε are the turbulent Prandtl numbers for k and ε. $C_{\varepsilon 1}$ and $C_{\varepsilon 2}$ are the unknown constant coefficients. Those constants have the following values (Fluent User's Guide 2001) in the standard *k*-ε model of ANSYS Fluent,

$$C_\mu=0.09,\quad \sigma_k=1.0,\quad C_{\varepsilon 1}=1.45,\quad C_{\varepsilon 2}=1.90,\quad \sigma_\varepsilon=1.30\,. \tag{47}$$

These constant values have been determined from experiments for fundamental turbulent flows including common shear flows like boundary layers, mixing layers and jets as well as for decaying isotropic grid turbulence. The standard *k*-ε model was found to work reasonably well for a wide range of wall-bounded turbulent flows and free shear turbulent flows. Therefore, I adopted this turbulent model in the simulations and the results will be presented in the later section.

2.3.2 Flow solvers

ANSYS Fluent as the primary tool used in the present study is based on the finite volume method. The computational domain is discretized into a finite set of control volumes and the governing equations, i.e. conservation equations for mass, momentum, and energy, are solved on the control volumes (Fluent Theory Guide 2013).

For the incompressible flow, the pressure-based approach is normally employed. There are two pressure-based solver algorithms available in ANSYS Fluent as the pressure-based segregated algorithm and pressure-based coupled algorithm. The segregated algorithm is memory-efficient and, however, the convergence is relatively slow because the equations are solved in a decoupled way. The coupled algorithm solves coupled equations and needs 1.5-2 times memory more than the segregated algorithm. However, the convergence is greatly enhanced compared with the segregated algorithm. Therefore, the user can choose the algorithm based on the research problem and computing capability. The detailed differences between the two algorithms, please refer to the guide of ANSYS Fluent (Fluent Theory Guide 2013).

3 Results and Discussion

This chapter presents the computational details, including mesh and numerical setup, and numerical results of planar channel flow without and with battens driven by wind and natural convection. The laminar flow of planar channel flow has been validated by a comparison with theoretical results. Moreover, a grid convergence study of channel flow with battens on the generated mesh has been carried out.

All parameters of the numerical simulations are chosen based on the experimental test of the ventilated roof by Gullbrekken et al. (2017) and Hansen (2016). The model sketch of the ventilated roof is shown in figure 3.1 and we focus on the central region.

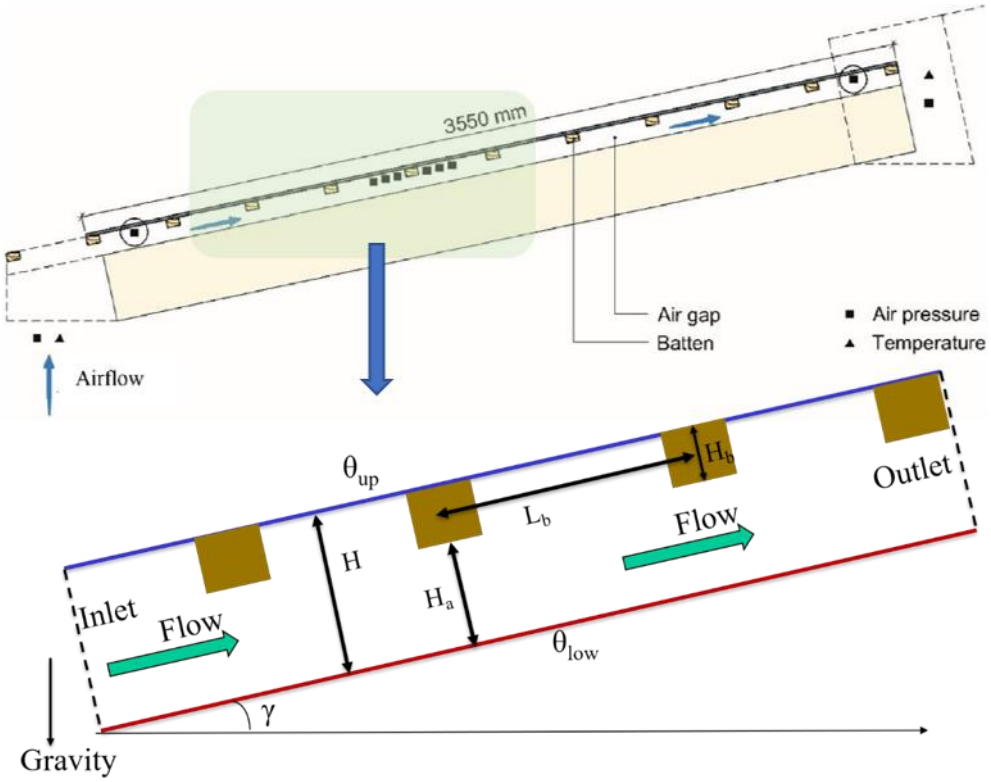

Figure 3.1: A sketch of a flow passing through a pitched roof model.

Table 3.1: Experimental parameters of the pitched roof test (Gullbrekken et al. 2017).

Test parameters	**Values**
Air gap height H_a (m)	0.023, 0.036, 0.048
Battens height H_b (m)	0.03, 0.036, 0.048
Batten center-to-center distance L_b (m)	0.35
Air velocity below battens U_b (m/s)	0.20, 0.40, 0.60, 0.80

3.1 Planar Channel Flow with Smooth Walls

In this subsection, I will study planar channel flows without battens as a reference case. The effect of inflow velocity, which is proportional to the Reynolds number with a fixed channel height, on the flow behavior is examined first. Furthermore, I will study the effect of the temperature difference between the upper and lower wall and the pitch angle of the roof on the natural convection and the mean flow in the streamwise direction.

3.1.1 Wind-driven flow

According to the experimental measurement (Gullbrekken et al. 2017), the corresponding bulk Reynolds number defined as $Re = U_b H / v$ is ranging from about 500 to 5000 with neglecting the battens. Here U_b is the bulk velocity (mean streamwise velocity) and H is the channel height. In this range, the flow can be turbulent (Re > 2900) or laminar (Re < 2300). Accordingly, I designed the simulation cases summarized in table 3.2. The fluid is air at 15 °C and one atmosphere pressure. Fluid dynamic viscosity and density are 1.81×10^{-5} Ns/m^2 and 1.225 kg/m^3, respectively. The simulation is 2D steady and using the pressure-based solver. The spatial discretization for momentum equation employs a second-order upwind scheme.

As shown in table 3.2, the cases S-1, S-2 and S-3 are laminar flows but the S-3 is close to the transition from laminar to turbulent flow. The case S-4 is a turbulent flow. Here, the computation for cases S-1, S-2 and S-3 are based on a laminar solver. S-4 is computed by using RANS turbulent model.

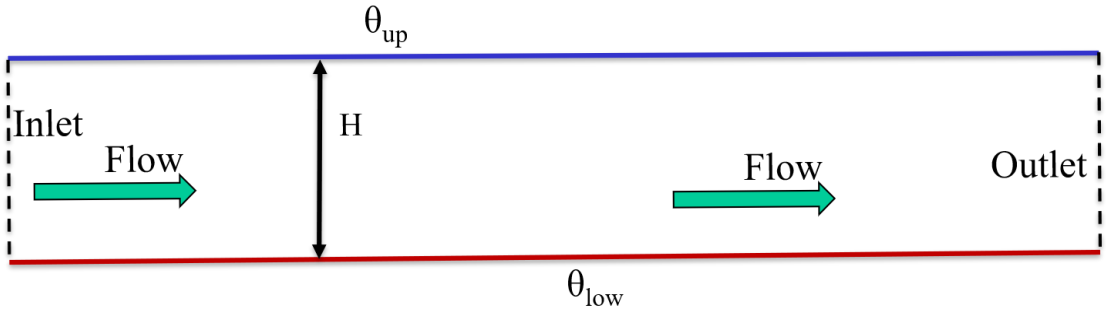

Figure 3.2: Sketch of a planar channel flow with smooth walls. H is the channel height and θ_{low} and θ_{up} are the temperature at the low and upper wall.

Table 3.2: Simulation parameters of channel flow without battens and without natural convection. L_x is the channel length and H is the channel height. N_x and N_y are the number of grid nodes in the streamwise and wall-normal direction, respectively.

Case ID	Mean velocity (m/s)	Domain (m)	Mesh: grid nodes	Re
S-1	0.2	$L_x \times H = 0.6 \times 0.06$	$N_x \times N_y = 500 \times 100$	774
S-2	0.4	$L_x \times H = 0.6 \times 0.06$	$N_x \times N_y = 500 \times 100$	1548
S-3	0.6	$L_x \times H = 0.6 \times 0.06$	$N_x \times N_y = 500 \times 100$	2322
S-4	0.8	$L_x \times H = 0.6 \times 0.06$	$N_x \times N_y = 500 \times 100$	3097

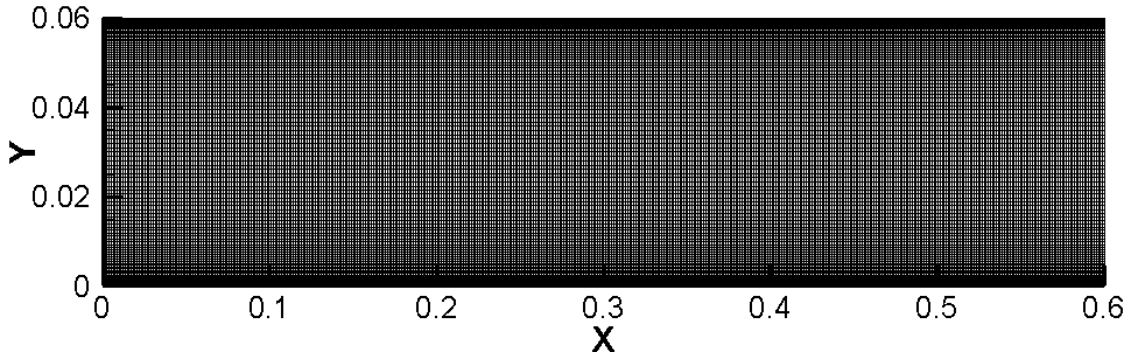

Figure 3.3: Cartesian mesh of the computation domain.

As shown in Figure 3.3, the mesh used in the simulations is a Cartesian grid and the size of the mesh is 500 grid nodes and 100 grid nodes in the streamwise and wall-normal direction, respectively. The mesh near the upper and lower wall is refined to reliably resolve the velocity gradient in the vicinity of the walls.

First, I tested two sets of boundary conditions (BC) for validating the simulation. The first set of BC is *velocity inlet* condition applied at the inlet and *outflow* boundary conditions imposed at the outlet. The second set of BC is a *periodic condition* at the inlet and outlet. In both sets of BC the upper and lower walls are *non-slip*. I performed two simulations with the two set BCs and as shown in figure 3.4. The streamwise velocity of the first simulation with inlet and outflow BC needs to develop at the inlet part and the fully developed flow in the downstream section is identical to the simulated results with the periodic BC, which means that both BCs work fine and can be used in the present study. The periodic BC avoids the developing stage in the first part and, therefore, in the following I use the periodic boundary condition for the rest simulations in this subsection.

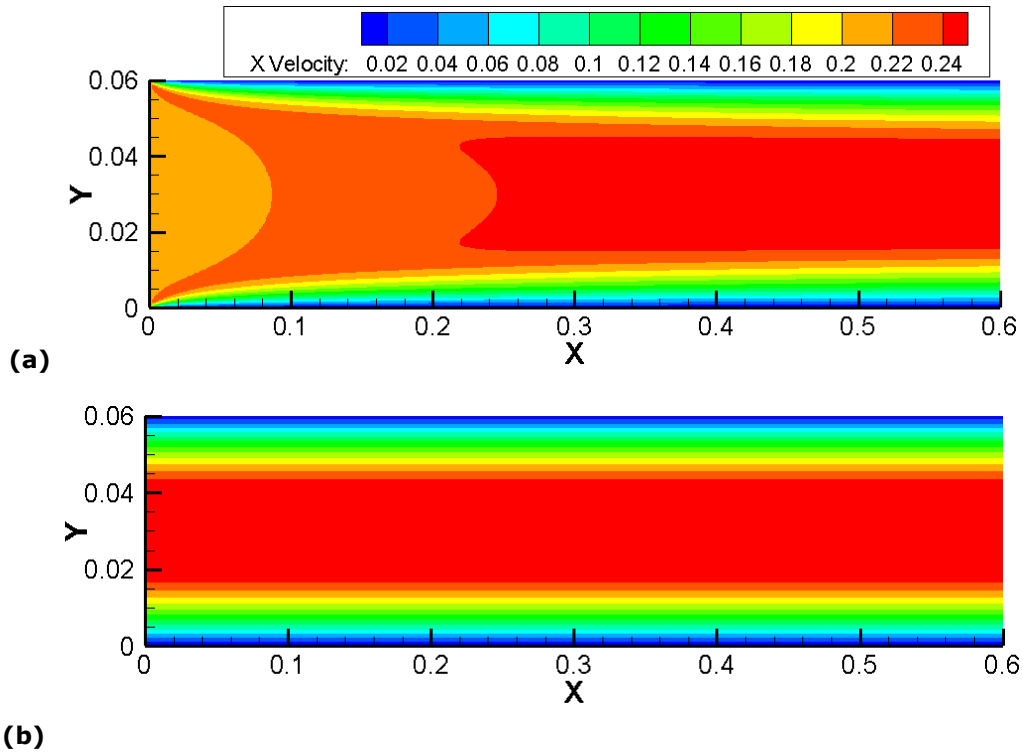

Figure 3.4: Contour of the streamwise velocity at Re = 774. (a) First set of BC: velocity inlet and outflow outlet; (b) Second set of BC: periodic boundary condition.

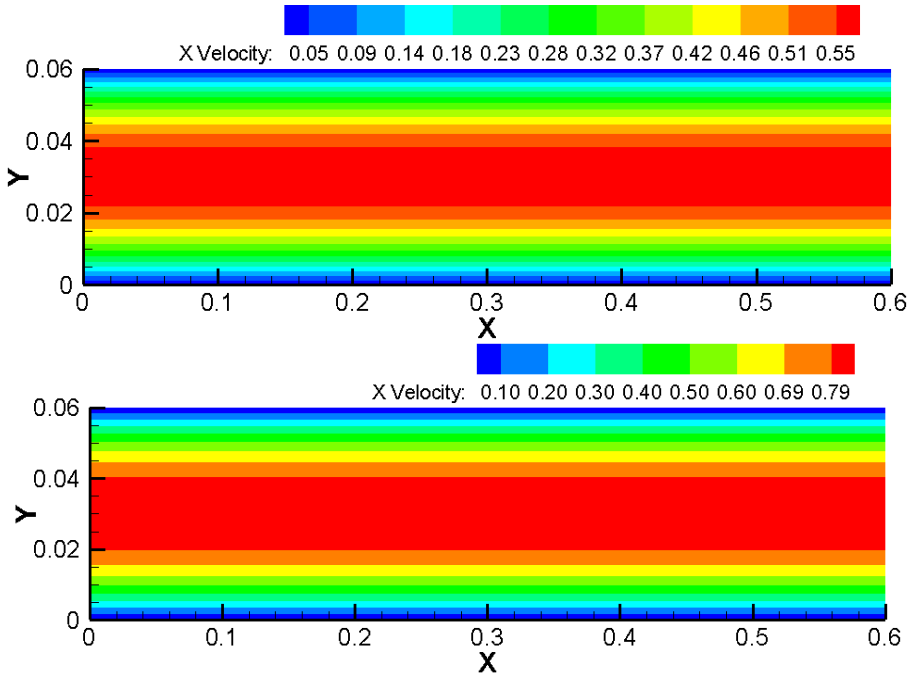

Figure 3.5: Contour of the streamwise velocity at Re = 1548 and 2322.

In addition, note that the channel height H is fixed for all cases as 0.06 m. For the cases of S-1 to S-4, the inflow velocity is ranging from 0.2 m/s to 0.8 m/s and the exact corresponding Reynolds number is given in table 3.2. Note that the temperature at the lower and upper wall is the same in the four cases and the natural convection is thus not included. First of all, I examine the Reynolds number effect on the laminar flows at Re = 1548 (S-2) and 2322 (S-3). Figure 3.5 shows the contour of the streamwise velocity and as we should expect, the flow is steady and the velocity is independent with the streamwise location. The change of velocity is abrupt in the near-wall region, which results in significant velocity gradients. The Reynolds number effect only influences the magnitude of velocity but the velocity pattern is obviously keeping the same, which is consistent with the theory of laminar flow (see Chapter 2).

With a higher Reynolds number, the case S-4 with Reynolds number Re = 3097 is in the turbulent regime. Therefore, with a periodic boundary condition at the inlet and outlet, I use the standard k-ω turbulence model with low-Reynolds number correction for modelling the turbulence shear stresses. The simulation is 2D steady and mesh is the same as the other laminar cases. It should be noted that the simulation of turbulent flows in present study takes a longer time than the simulation of laminar flows.

In figure 3.6 I extract the contour of the streamwise velocity, turbulent kinetic energy and the static pressure. The streawmise velocity of turbulent flow has a different pattern compared with the case of laminar flow in figure 3.5. The velocity change in the near-wall region is more significant in turbulent flow and therefore leads to stronger velocity gradients. The turbulent kinetic energy represents the strength of the velocity fluctuations and we can see that the maximum turbulent intensity occurs in the near-wall region, where is normally called the buffer region. In the channel center region the turbulence is relatively weak. The distribution of static pressure is not smooth, which indicates that the turbulence fluctuation affects the static pressure.

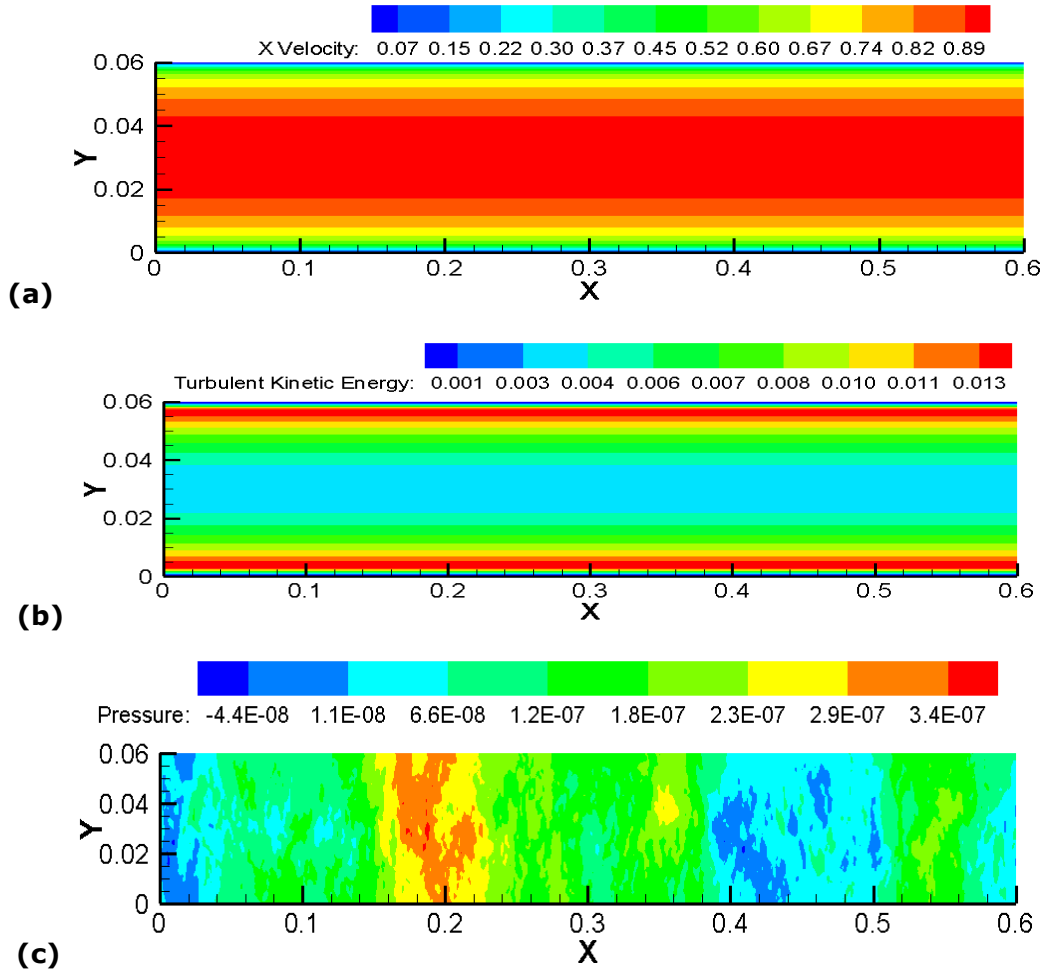

Figure 3.6: Contour of (a) the mean streamwise velocity, (b) turbulent kinetic energy and (c) static pressure in the case S-4 at Re = 3097.

In figure 3.7 I extract the mean streamwise velocity of the cases S-1 to S-4 and plot them in the wall-normal direction. It is clear that the magnitude of velocity varies from the lower wall to the upper wall and the profile is symmetric with the channel centerline. The velocity grows as the Reynolds number increases. The cases S-1, S-2 and S-3 are laminar flow, whose velocity profile is distinctly different from that of turbulent flow case S-4. The turbulent flow case has a larger velocity gradient near the walls than the laminar flow cases. All of those results are reasonably consistent with the theory but a quantitative comparison is needed to validate the accuracy of the results of current computations. Therefore, in the following I move on to check the friction factor of the four cases.

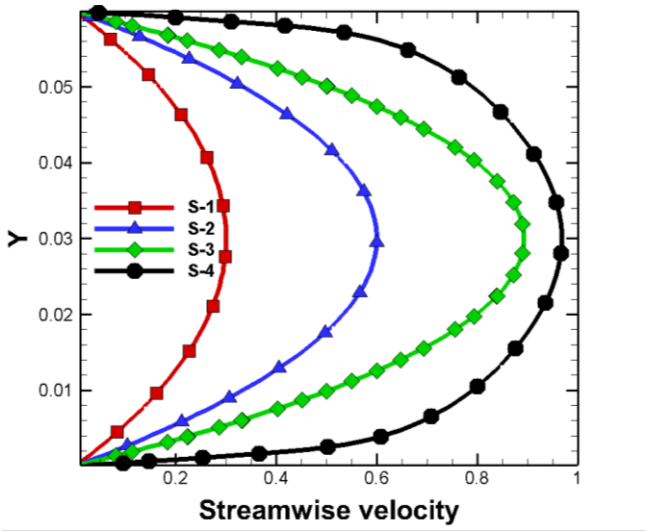

Figure 3.7: Profiles of the mean streamwise velocity in the wall-normal direction at different air speeds.

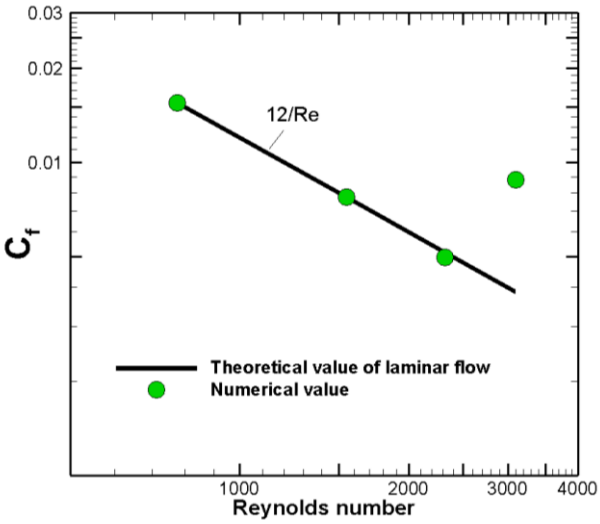

Figure 3.8: Friction factor versus Reynolds number. The solid line represents the theoretical friction factor C_f following $C_f = 12/\mathrm{Re}$. The green circles are the numerical results of S-1, S-2, S-3 and S-4.

For the laminar channel flow, the theoretical friction factor (also called friction loss coefficient) follows $C_f = 12/\mathrm{Re}$ was derived in Chapter 2. The friction factor, as a measure of the resistance to airflow, is defined as the ratio of the shear stress and the dynamic pressure. Since the shear stress is dependent on the pressure gradient and dynamic viscosity, the friction factor also reflects the pressure loss, which is mainly caused by viscous friction. Figure 3.8 shows the numerical results of friction factors at different Reynolds number and compared with the theoretical friction factor of laminar channel flow. It is clear that my numerical results of laminar flow case S-1, S-2 and S-3 are in very good agreement with the theory, which indicates the simulation is reliable. The theory is derived based on laminar flow assumption and it is natural that the numerical value of turbulent flow S-4 is greatly higher than the theory (log-scale used in the figure), which indicates the friction loss of turbulent flow is more significant.

3.1.2 Channel flow driven by natural convection

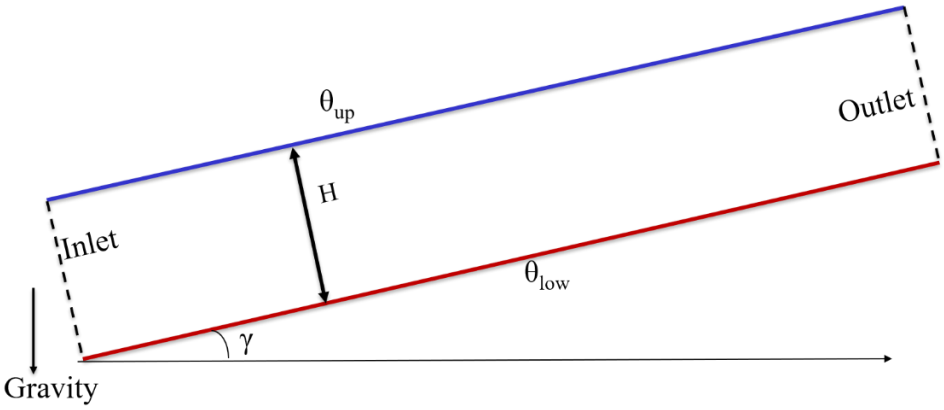

Figure 3.9: Sketch of a pitched channel with natural convection. H is the channel height and θ_{low} and θ_{up} are the temperature at the lower wall and upper wall, respectively. Here γ stands for the pitch angle as the relative angle between horizontal direction and the streamwise direction.

Table 3.3: Simulation parameters of natural convection in a channel. L_x is the length of computation domain. N_x and N_y are the grid nodes in the streamwise and wall-normal direction, respectively. Δθ stands for the temperature difference between the two walls.

Case ID	Inclination γ (degree)	Comp. domain (m)	Mesh: grid nodes	$\Delta\theta = \theta_{low} - \theta_{up}$ (K)
N-1	0.0	$L_x \times H = 0.3 \times 0.03$	$N_x \times N_y = 500 \times 100$	2
N-2	0.0	$L_x \times H = 0.3 \times 0.03$	$N_x \times N_y = 500 \times 100$	10
N-3	10.0	$L_x \times H = 0.3 \times 0.03$	$N_x \times N_y = 500 \times 100$	2
N-4	45.0	$L_x \times H = 0.3 \times 0.03$	$N_x \times N_y = 500 \times 100$	2
N-5	45.0	$L_x \times H = 0.3 \times 0.03$	$N_x \times N_y = 500 \times 100$	10

In the present subsection the two factors, i.e. inclination angle γ, and temperature difference Δθ, will be explored. I design four cases to be performed, and all simulation parameters are summarized in table 3.3. Note that compared with the simulations in 3.1.1, there is no flow driven by wind or pressure gradient and the flow motion is only driven by the natural convection.

Here, I set zero bulk velocity without the pressure gradient or inlet velocity and periodic boundary condition is used at the inlet and outlet. Non-slip boundary condition is imposed at the two solid walls and the distance between two walls is 0.03m for all cases. The temperature at the upper wall and lower wall is $\theta_{up} = 298\ K$ and $\theta_{low} = 300\ K$ or $308\ K$, respectively. In the simulation, the fluid is air at one-atmosphere pressure and 15 °C. The air density is about 1.225 kg/m^3 and the dynamic viscosity is $1.83\times10^{-5}\ Ns/m^2$. The energy equation is solved together with mass and momentum equations. In such a condition, the thermal conductivity of air is 0.0263 w/mk and the thermal expansion coefficient is 0.00366 K^{-1}.

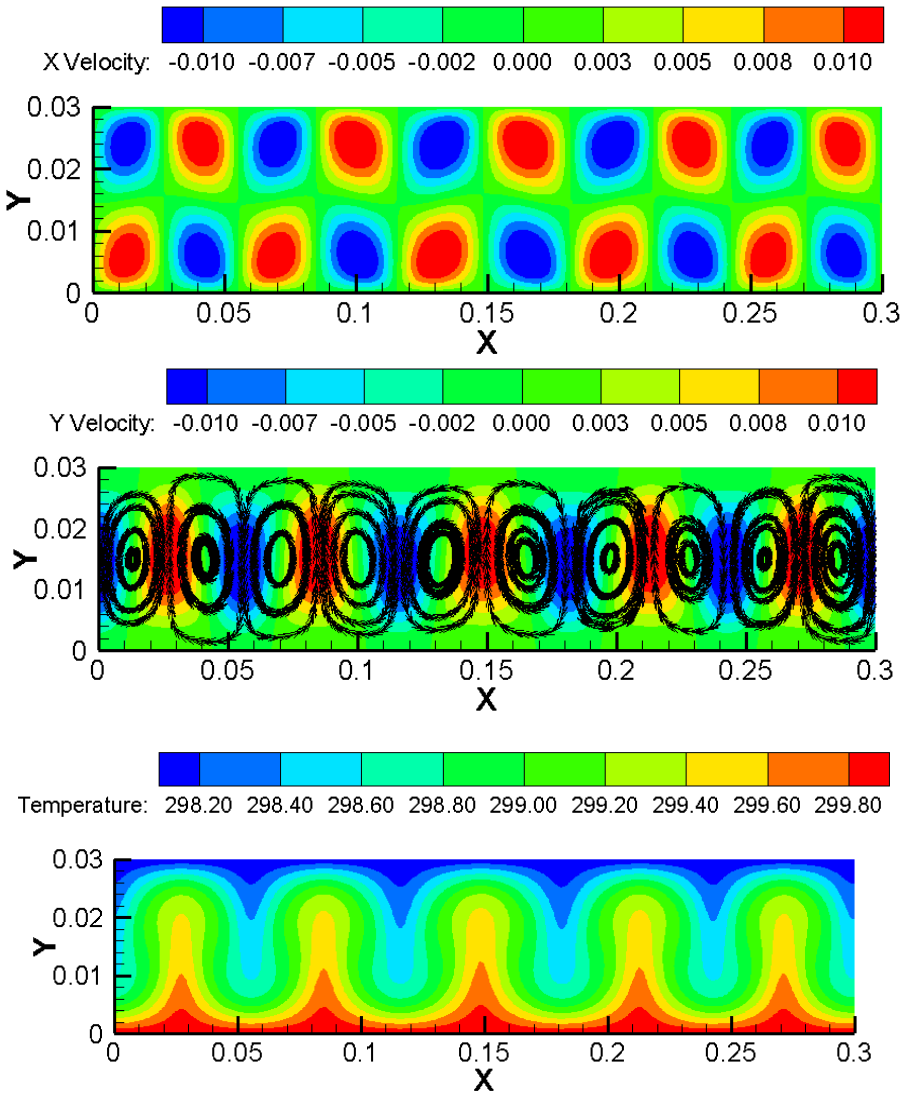

Figure 3.10: Contour of (a) streamwise and (b) the wall-normal velocity, and (c) temperature contour of natural convection in a channel with temperature difference Δθ = 2 K and an inclination angle γ = 0 degrees (Case N-1). The black lines in panel (b) are the streamlines to visualize the convection rolls.

Regarding the case N-1 with a 2 *K* temperature difference and zero pitch angle, the corresponding Rayleigh number Ra about 5000, which means that the natural convection occurs but the flow is laminar. As mentioned in Chapter 2, the natural convection is a buoyancy-driven flow due to the presence of temperature gradient (Barna et al. 2017). Figure 3.10 (a) shows the streamwise velocity contour and it is interesting that the contour consists of two layers of cell pairs with positive and negative velocity. Similarly, the velocity in the wall-normal direction as shown in figure 3.10 (b) also has the pattern of cell-pairs with negative and positive y-velocity. In addition, I included the streamlines in figure 3.10 (b), which clearly show the two-dimensional convection rolls. The nearby rolls are counter-rotating. Such kind of rotational motion of airflow enhances the heat transfer from the lower wall to the top wall, which can been seen in the temperature contour plot of figure 3.10(c). The higher and lower temperature regions are located between the counter-rotating rolls and dependent on the direction of airflow motion in the wall-normal direction.

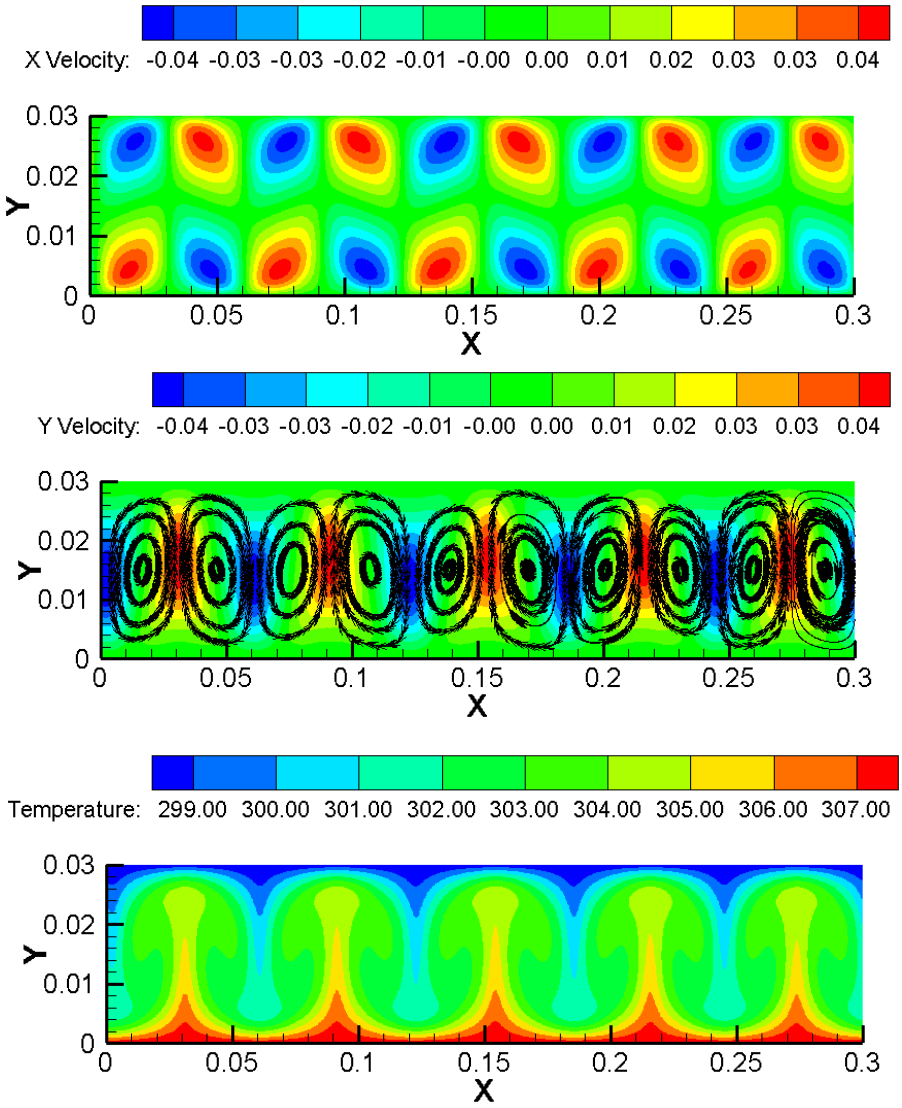

Figure 3.11: Contour of (a) streamwise and (b) the wall-normal velocity, and (c) temperature contour of natural convection in a channel with temperature difference Δθ = 10 K and an inclination angle γ = 0 degrees (Case N-2). The black lines in panel (b) are the streamlines to visualize the convection rolls.

Regarding the case N-2 with a 10 *K* temperature difference and zero pitch angle, the corresponding Rayleigh number Ra about 25000. Compared with the earlier case N-1, the temperature difference is enlarged and therefore the driven force due to the natural convection is more significant. First, the velocity magnitude is larger than the results of N-1. Because of the enhanced flow motion, the heat transfer is more significant and the mean temperature is higher than that of N-1 (see Figure 3.10 c). Second, the size of convection cell seems smaller but the number of the convection rolls is the same as N-1. Considering the practice case of ventilated roof, according to the preliminary results of N-1 and N-2, we can see that the airflow driven by the natural convection enhances the heat transfer from the lower wall to the top wall, which is a negative factor if a designer wants to avoid or reduce the snow melting. On the other hand, the temperature difference is proportional to the natural convection and indirectly augments the heat transfer between two walls. In the following, the effect of channel inclination will be examined.

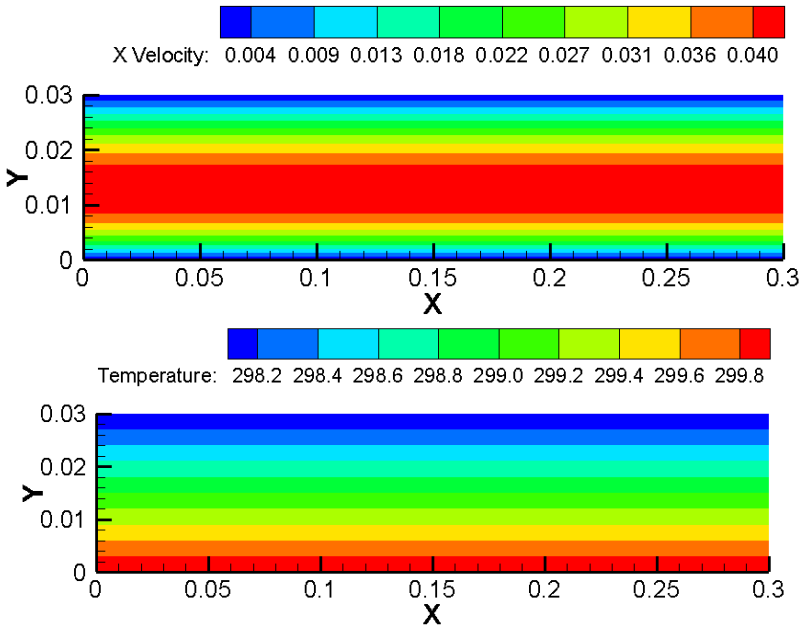

Figure 3.12: Contour of (a) streamwise velocity and (b) temperature contour of natural convection in a channel with temperature difference $\Delta\theta = 2\ K$ and an inclination angle γ = 10 degrees (Case N-3).

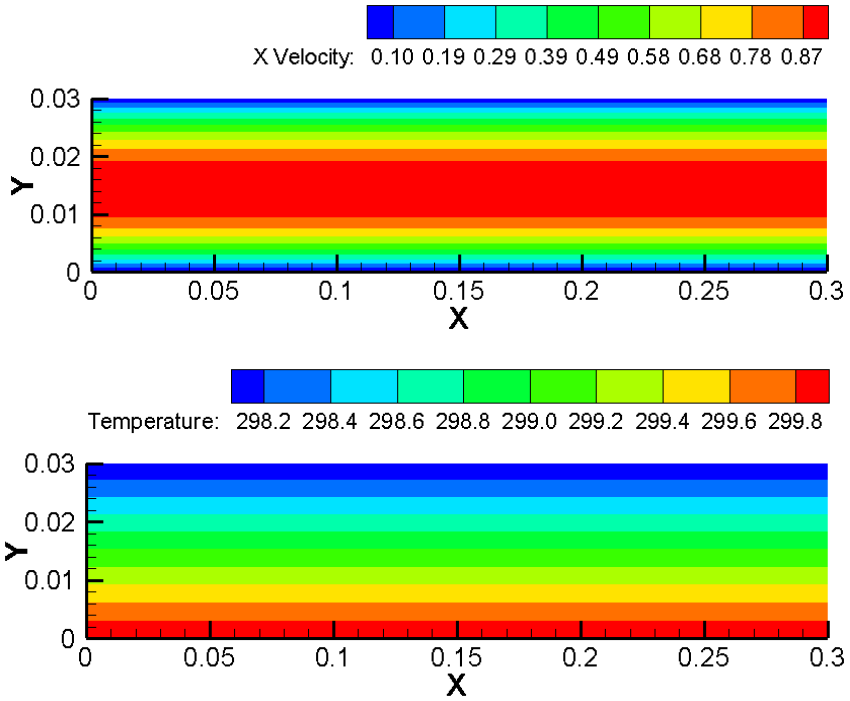

Figure 3.13: Contour of (a) streamwise velocity and (b) temperature contour of natural convection in a channel with temperature difference $\Delta\theta = 2\ K$ and an inclination angle γ = 45 degrees (Case N-4).

In the case of N-3, the pitch angle increases from 0 to 10 degrees compared with N-1. As shown in figure 3.12, it is surprising to observe that all convection rolls are diminished. The flow pattern is, therefore, distinctly different from the earlier cases of N-1 and N-2. The contour of streamwise velocity only depends on the location in the wall-normal direction and looks identical to the wind-driven case of laminar flow (for instance the case of S-1). However, an obvious difference is the flow is not symmetric about the centerline of the channel. The contour of temperature is also greatly different from the case with zero inclination angle and the temperature seems linearly varied from the lower wall to the upper wall. Therefore, the effect of pitch angle seems very significant that, even with a small pitch angle, the natural convection rolls are all disappeared.

In the view of the pitched ventilation roof, the inclination design is essential to reduce the heat transfer induced by the natural convection rolls.

Furthermore, I increase the pitch angle from 10 to 45 degrees in the case N-4 to examined the effect of a large pitch angle. The numerical results are given in figure 3.13 and I find that the flow contours are qualitatively similar to the case N-3. However, with a larger pitch angle, the velocity is obviously augmented, which is a positive effect to reduce the heat transfer and remove the moister air in the roof. Therefore, in the view of pitch roof design, the current results indicate that a larger pitch angle will enhance the streamwise air velocity, which is actually driven by the temperature difference.

In the end, I extracted the profiles of mean streamwise velocity for the cases S-3, S-4, and S-5. The comparison is shown in figure 3.14. The results reveal that the effect of pitch angle is more significant than the effect of temperature difference on the enhancement of streamwise air velocity. Moreover, once again the asymmetric distribution of streamwise velocity is seen for all three cases. The peak location is shifted towards to the lower wall, which has a higher temperature.

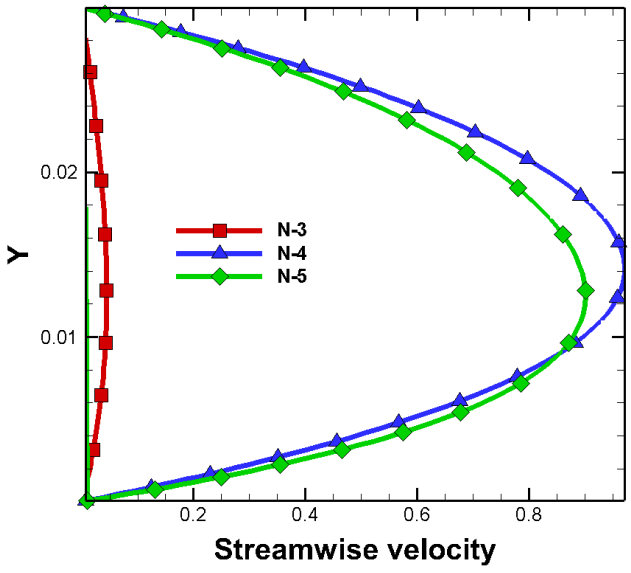

Figure 3.14: Streamwise velocity profile of natural convection in a channel with temperature difference Δθ = 2 *K* and 10 *K* and an inclination angle γ =10 and 45 degrees.

3.1.3 Wind driven flow with natural convection

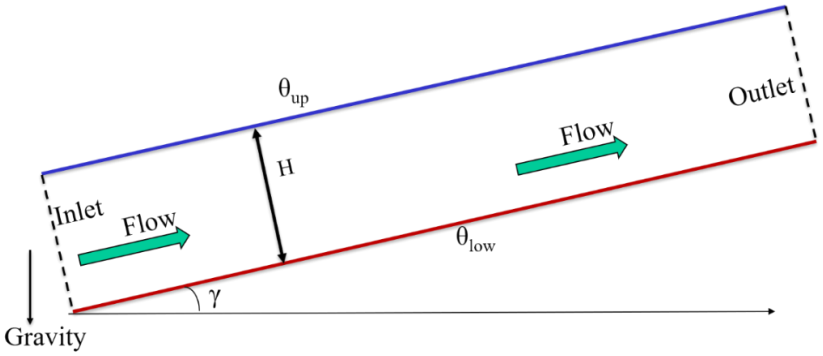

Figure 3.15: Sketch of channel driven by both wind and natural convection. H is the channel height and θ_{low} and θ_{up} are the temperature at the lower wall and upper wall, respectively. Here γ stands for the pitch angle as the relative angle between horizontal direction and the streamwise direction.

Table 3.4: Simulation parameters of natural convection in a wind-driven channel flow. L_x is the length of computation domain. N_x and N_y are the grid nodes in the streamwise and wall-normal direction, respectively. Δθ stands for the temperature difference between the two walls.

Case ID	Inclination γ (degree)	Inflow velocity (m/s)	Comput. Domain (m)	$\Delta\theta = \theta_{low} - \theta_{up}$ (K)
WN-1	0.0	0.02	$L_x \times H = 0.3 \times 0.03$	10
WN-2	0.0	0.2	$L_x \times H = 0.3 \times 0.03$	10
WN-3	5.0	0.2	$L_x \times H = 0.3 \times 0.03$	10
WN-4	10.0	0.2	$L_x \times H = 0.3 \times 0.03$	10
WN-5	45.0	0.2	$L_x \times H = 0.3 \times 0.03$	10
WN-6	60.0	0.2	$L_x \times H = 0.3 \times 0.03$	10

After a detailed analysis in 3.1.1 and 3.1.2, the effect of wind-driven and the effect of natural convection have been examined separately. In the present subsection, I combine the two driven-forces together in the channel flow and such flow configuration is therefore close to the realistic condition of a pitched ventilated roof flow.

The simulation parameters are summarized in table 3.4. The mesh is the same as that used in subsection 3.1.1 and 3.1.2. I choose bulk velocity as 0.02 m/s and 0.2 m/s. The *velocity inlet* condition is applied at the inlet and *outflow* boundary condition is imposed at the outlet. The *non-slip* boundary condition is adopted at the two solid walls and the distance between two walls is 0.03m for all cases. The temperature at the upper wall and lower wall is $\theta_{up} = 298\ K$ and $\theta_{low} = 308\ K$, which gives 10 *K* temperature difference. The pitch angle is 0, 5, 10, 45 and 60 degrees. In the simulation, the fluid is air at one atmosphere pressure and 15 °C. The air density is about 1.225 kg/m^3 and the dynamic viscosity is 1.83×10^{-5} Ns/m^2. The energy equation is solved together with mass and momentum equations. In such a condition, the thermal conductivity of air is 0.0263 *w/mk* and the thermal expansion coefficient is 0.00366 K^{-1}.

The computation is based on a laminar solver and the momentum and energy conservations equations are integrated using a second-order upwind scheme.

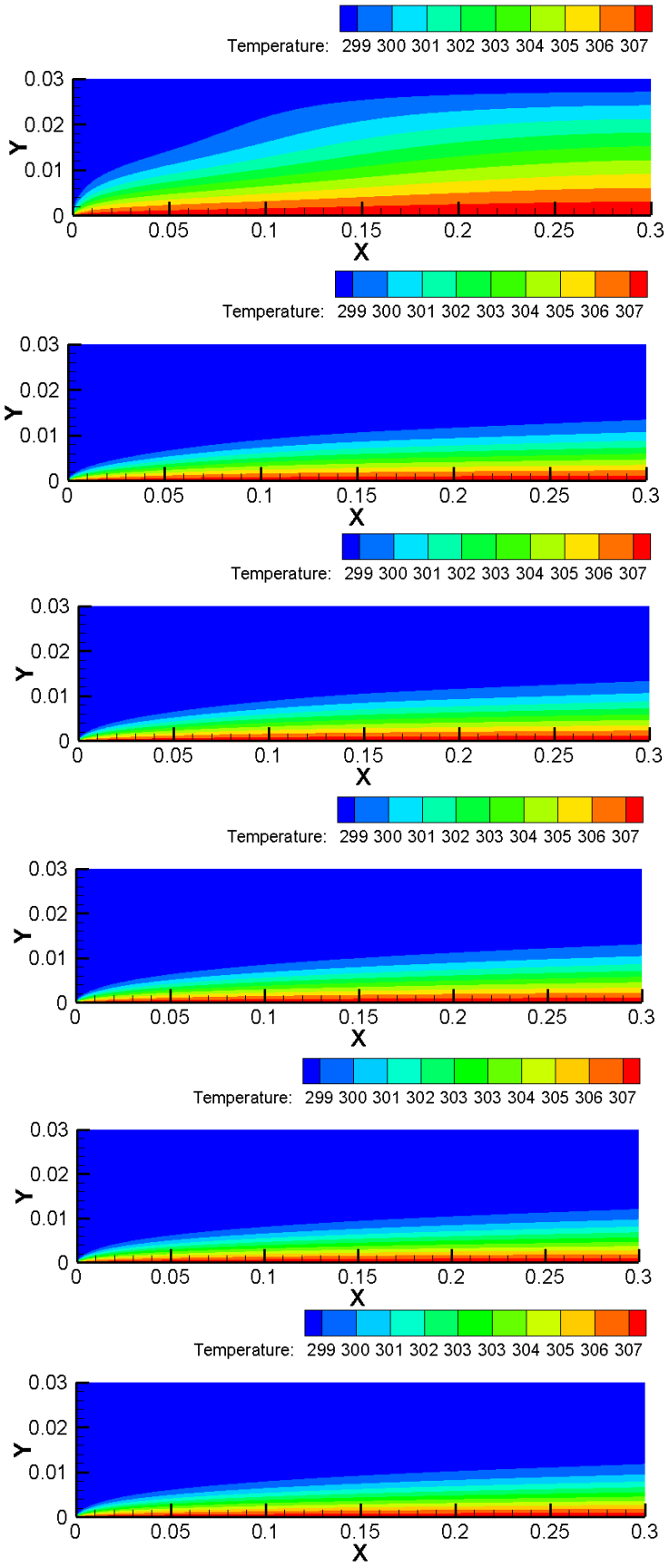

Figure 3.16: Temperature contours of cases WN-1 to WN-6.

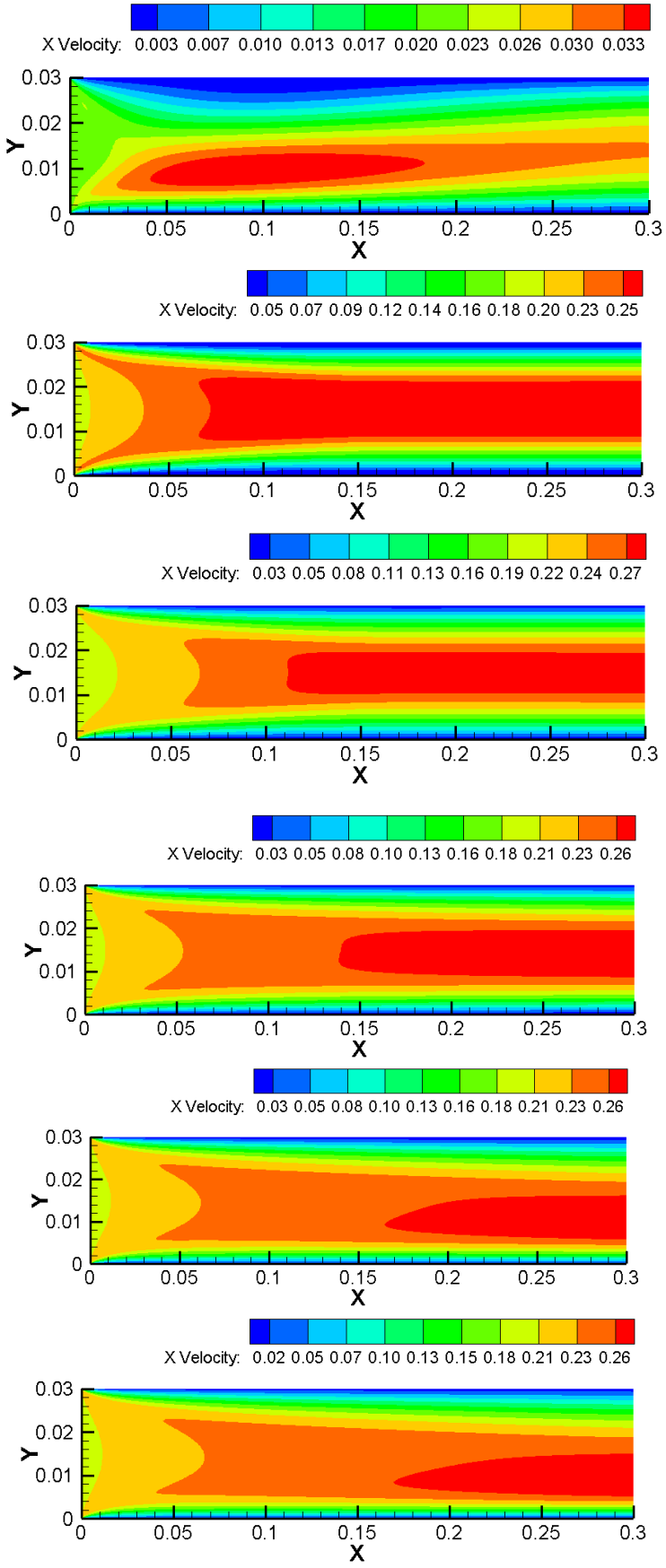

Figure 3.17: Streamwise velocity contours of cases WN-1 to WN-6.

First, the temperature contours of the six cases are shown in figure 3.16. According to the temperature distribution, I find that the first case WN-1 with a lower inlet velocity of 0.02 m/s shows a stronger heat transfer than other cases with a mean velocity of 0.2 m/s. It indicates that the increase of mean airflow velocity suppresses the heat transfer, which can be understood that the air can bring the heat out of the channel faster with a larger velocity. In the rest cases of WN-2 to WN-6, the mean velocity is 0.2 m/s and temperature difference is fixed as 10 K with only adjusting the pitch angle from 0 to 60 degrees. However, the temperature contours of WN-2 to WN-6 are similar, which reveals that the role played the temperature difference is insignificant on the heat transfer in the parameter-range considered herein.

Second, I examine the velocity distribution of those six cases as shown in figure 3.17. The velocity contour of WN-1 looks different from other cases, which is due to the small inlet air velocity. The effect of natural convection and wind-driven inlet velocity competes and results in such velocity distribution. In the rest cases, the wind-driven effect becomes dominant with 10 times larger inlet velocity and the flow contour is similar to the earlier cases of wind-driven laminar channel flow. However, the natural convection, which is caused by the temperature difference, also plays a non-negligible role and causes the asymmetric distribution of the streamwise velocity that the peak velocity is located closer to the lower wall, which has a higher temperature. Again, the effect of increasing the pitch angle on the velocity distribution is insignificant. Therefore, in this condition of combing the wind-driven and the natural convection, the pitch angle plays a less important role.

In the end, I extract the profiles of the streamwise velocity and plot them in the wall-normal direction as shown in figure 3.18. The curves are consistent with the contour plots in earlier figures. The case of WN-1 has the minimum velocity because of the small inlet velocity. The other curves are similar and the effect of pitch angle can be seen by the shift of the peak location from the channel center to the lower wall. The shift towards the lower wall is monotonical with increasing the pitch angle from 0 to 60 degrees.

As a summary, the results in Section 3.1. show that the thermal convection plays a less important role and Rayleigh-Bernard instability is suppressed if there is mean airflow driven in the streamwise direction (even though the mean velocity is relatively small). Moreover, the effect of inclination angle is negligible as long as there is wind-driven flow. However, one should note that if the wind-driven flow is not present, the natural convection effect is essentially dominant and the pitch angle is of importance.

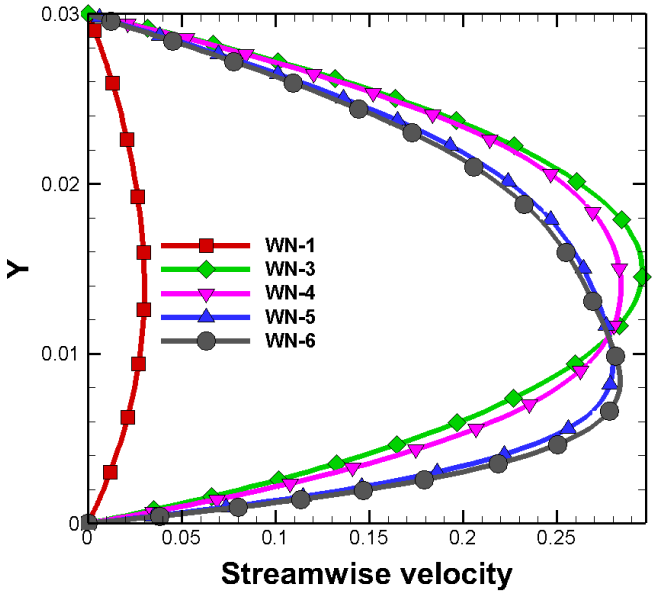

Figure 3.18: Streamwise velocity profile of a channel flow with wind-driven and natural convection. The temperature difference Δθ = 10 *K* and an inclination angle γ = 0 to 60 degrees.

3.2 Channel Flow with Sharp-Edged Battens

In this section, I performed a series of numerical simulations of channel flows with sharp-edged battens mounted on the upper wall. The main objective is to investigate the effect of battens on the airflow friction, which is a crucial factor considered in the design of a pitched ventilated roof. Based on the numerical results, I focus on the effects of inlet velocity, temperature difference and the pitch angle on the flow behavior and pressure loss in the channel.

3.2.1 Computation model and mesh

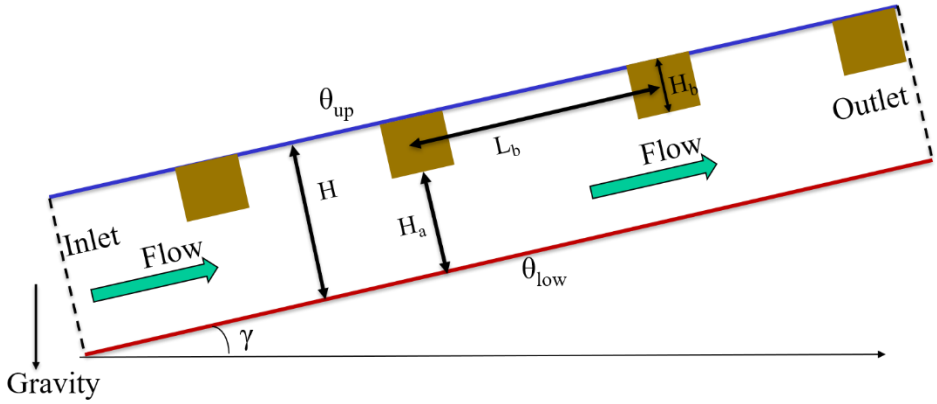

Figure 3.19: Sketch of a channel flow with sharp-edged battens. H is the channel height and θ_{low} and θ_{up} are the temperature at the lower wall and upper wall, respectively. Here γ stands for the pitch angle as the relative angle between horizontal direction and the streamwise direction

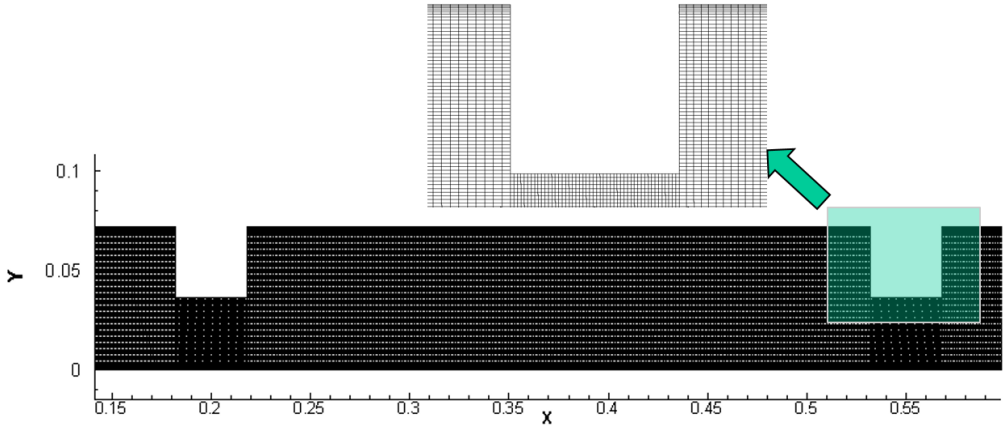

Figure 3.20: Mesh of the channel with sharp-edged battens.

As shown in figure 3.19, the computation model is two dimensional and the parameters, for instance, channel height and batten size, are based on the experimental measurement by Gullbrekken et al. (2017). Figure 3.20 shows the mesh structure and similar to the cases of channel flow with smooth walls I adopted Cartesian mesh again and refine the mesh resolution near the solid walls and the battens to resolve the velocity gradients.

Similarly, I tested two sets of boundary conditions (BC), i. e. (1) velocity inlet, outflow outlet and non-slip condition at walls and at the surface of battens; (2) periodic boundary

inlet and outlet conditions, and non-slip boundary conditions at wall and at the surface of battens. According to the tests, the two sets BCs give similar results and in the rest of this subsection I adopted the periodic boundary condition, which is computationally more efficient and can provide the information of pressure gradient and friction factor in an easy way.

Following the CFD study by Gullbrekken et al. (2017), flow with battens is associated with large recirculation behind the battens and should be turbulent. I employ the κ-ε two equation turbulence model with standard wall function. The momentum and energy conservation equations are solved using a second-order upwind scheme. The equations of turbulent kinetic energy and dissipation rate are integrated using a first-order upwind scheme.

3.2.2 Grid-dependence test

Because of the complicated geometry of the computation model, the flow with battens requires high-quality mesh to resolve not only the near-wall flow behavior but also the separation vortex behind the batten. Therefore, we test two sets of mesh with different grid nodes to validate the grid-dependence of the numerical results. As shown in the table, the coarse case Mesh I has 26800 grid nodes and the finer case Mesh II has about two times more grid nodes as 49380 nodes. The direct comparison of the two mesh sets can be found in figure 3.21 and it is obvious that the Mesh II has a denser mesh than Mesh I. I run a test case by using the two meshes. The size of battens is 0.036 × 0.048 m (height × width) and the height of air gap is 0.023 m. The temperature difference is 10 K with a zero pitch angle. The mass flow rate is 0.014 kg/s, which corresponds to the bulk velocity of 0.2 m/s

First, I measure the mean pressure gradient ∇p through the channel by following the equation below,

$$\nabla p = \frac{\partial p}{\partial x} = \frac{p_1 - p_2}{L_b} \quad . \tag{48}$$

Here p_1 and p_2 are measured at point 1 in the front of a batten and point 2 behind the batten, respectively. The point 1 and point 2 to the batten center is $L_b/2$ and therefore, the mean pressure gradient can be computed in equation (48). In table 3.5, I got a very similar pressure gradient by using the two meshes. On the other hand, figure 3.22 shows the identical contour of streamwise velocity using the two different meshes. Therefore, those results indicate that the Mesh I with a coarse mesh can provide sufficient fine results independent of mesh resolution. I adopt the Mesh I in the rest computations to save computation cost.

Table 3.5: Test of grid independence.

Test case	**Mesh I**	**Mesh II**
Grid nodes	26800	49380
Pressure gradient ∇p	-0.5510	-0.5502

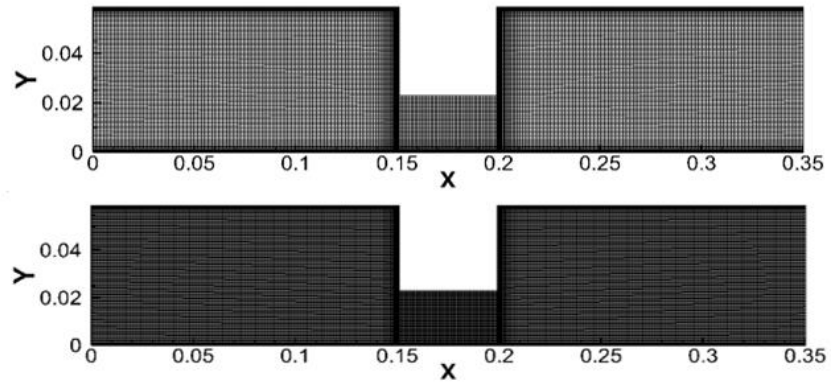

Figure 3.21: Two mesh sets, Mesh I (top panel) and Mesh II (low panel), with different resolution

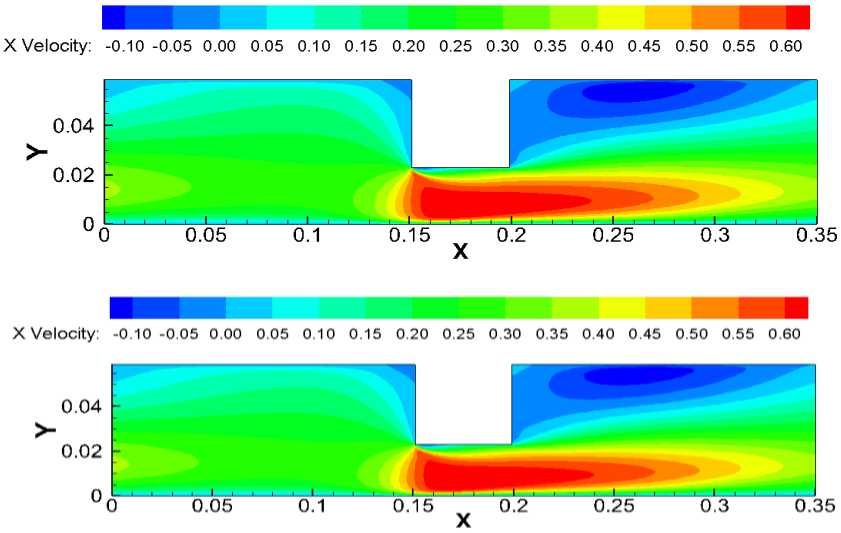

Figure 3.22: Contour of streamwise velocity by using Mesh I and Mesh II

3.2.3 Effects of inlet velocity, air-gap height, temperature difference and pitch angle

In the case of channel flow with battens, there are several factors, including bulk velocity, temperature difference, etc, to be considered. I design a series of simulations (as shown in table 3.5) to investigate the effects of those factors on the flow behavior, pressure gradient, friction coefficient and local loss coefficient. The calculation of the pressure coefficient is following equation (48). The friction coefficient C_f is computed by the following equation:

$$C_f = \frac{\tau_w}{1/2\rho U_b^2} \quad , \quad \tau_w = -\nabla p \frac{H}{2} \tag{49}$$

Here, U_b is the bulk velocity and τ_w is the stress on the wall. H is the channel height.

The local loss coefficient is defined following the work by Gullbrekken et al. (2017) as:

$$\xi = \frac{2\nabla p L_b}{\rho U_m^2} \quad , \quad U_m = \frac{Q}{A_b} \tag{50}$$

Here, U_m is given by the airflow rate Q (m^3/s) divided by the area of the cross section of the flow path under the battens A_b. Therefore, U_m is the mean velocity under the battens.

Table 3.6: Simulation parameters of channel flow with sharp-edged battens. The batten size is 0.036 × 0.048 m.

Case ID	γ (deg)	Bulk velocity (m/s)	Ha (m)	Mean velocity under battens (m/s)	Δθ (K)	Pressure gradient	Friction coefficient	Local loss coefficient
B-1	0.0	0.2	0.036	0.40	10	-0.246	0.361	0.879
B-2	0.0	0.4	0.036	0.80	10	-0.896	0.329	0.800
B-3	0.0	0.6	0.036	1.20	10	-1.937	0.316	0.769
B-4	45.0	0.2	0.036	0.40	10	-0.112	0.165	0.400
B-5	30.0	0.2	0.036	0.40	10	-0.152	0.223	0.543
B-6	0.0	0.2	0.023	0.51	10	-0.551	0.663	1.196
B-7	0.0	0.2	0.048	0.35	10	-0.150	0.257	0.700

First, the results of B-1, as a reference case, are shown in figure 3.23. It is well known that the flow friction, or fluid resistance, includes form drag and skin friction drag. The latter skin friction is caused by the viscosity of fluid, such as the viscous friction generated on the lower or upper wall of the channel. The form drag, or called pressure drag, arises because of the shape of the object. In the present case of channel flow with battens, there are both form drag and skin friction drag. The form drag is mainly caused by the presence of battens and as shown in figure 3.23 (b) the pressure difference in the frontward and backward of the batten contributes the major part of the form drag. The low pressure region on the backward side of the batten is due to the vortex separation as shown in figure 3.23 (a). I draw the streamlines and an obvious vortex is observed behind the batten. On the other hand, the velocity distribution is strongly dependent on the cross-section area that the streamwise velocity is significantly large under the batten. I also note that the temperature distribution is also influenced due to the presence of batten. A low temperature region can be seen behind the batten, which can be due to the low velocity in that region.

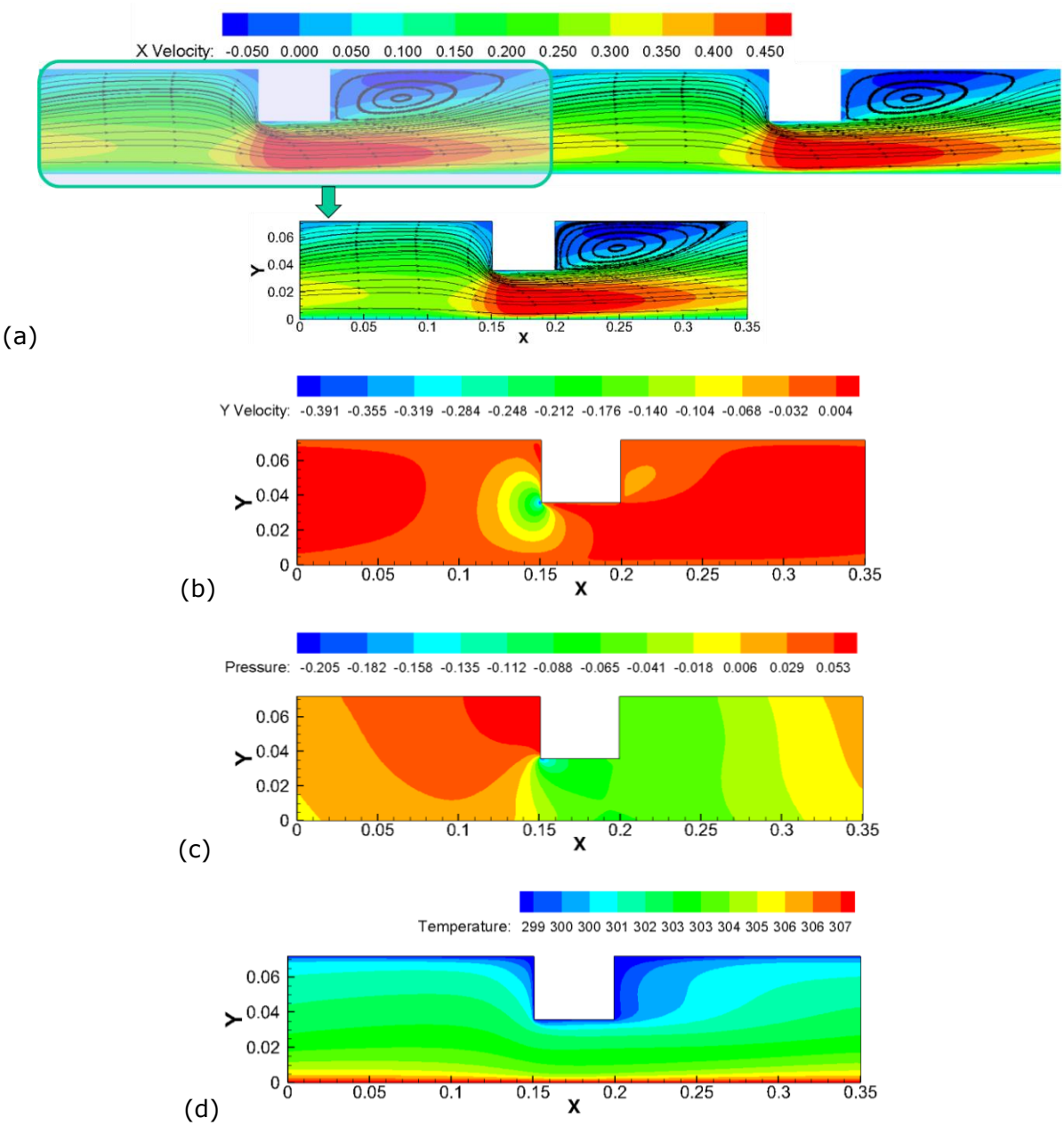

Figure 3.23: Contours of (a) streamwise velocity, (b) wall-normal velocity, (c) static pressure and (d) temperature of case B-1.

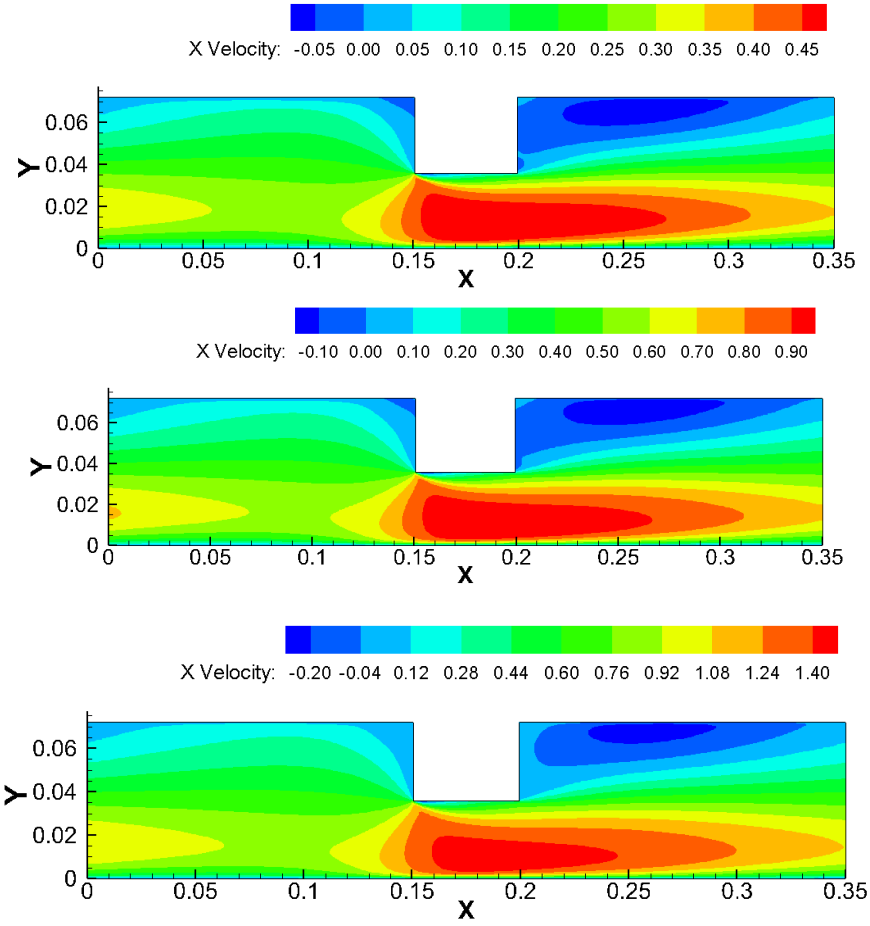

Figure 3.24: Contour of streamwise velocity for case B-1, B-2 and B-3 with bulk velocity ranging from 0.2 m/s to 0.6 m/s.

The streamwise contour of case B-1 to B-3 is shown in figure 3.20 with bulk velocity from 0.2 m/s to 0.6 m/s. The general distribution of all three cases looks similar and the major difference is the magnitude of the velocity that the B-3 has an obviously higher velocity than other cases. A minor difference is a small change of shape of the vortex region behind the batten. Even though the velocity distribution is similar but the pressure gradient changes from -0.246 (B-1) to -1.937 (B-3). An obvious reduction of both friction coefficient and local loss coefficient (more than 10%) is observed as the bulk velocity grows (see table 3.6), whose trend is consistent with the experimental measurement in Gullbrekken et al. (2017). Those findings indicate that the increase of bulk velocity or airflow rate can reduce the friction coefficient and reduce the local loss coefficient, which provides a positive effect in the realistic case of a ventilated roof.

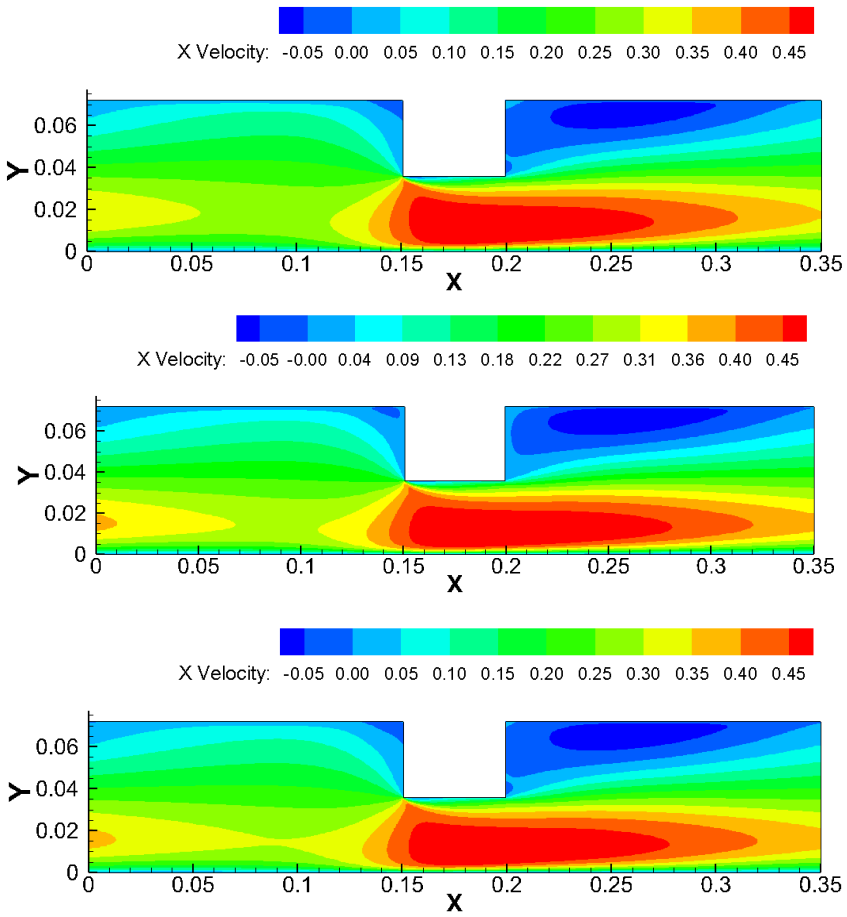

Figure 3.25: Contour of streamwise velocity for case B-1, B-4 and B-5 with pitch angle as 0, 45, 30 degrees, respectively.

In figure 3.25, I examined the contour of streamwise velocity for B-1, B-4 and B-5. All three cases are with the same bulk velocity 0.2 m/s but different pitch angles as B-1 with 0 degree, B-4 with 45 degrees and B-5 with 30 degrees. First, no obvious difference is observed in the distribution of velocity according to the contour plots. However, I find a significant reduction of friction coefficient and local loss coefficient as the pitch angle increases. The friction coefficient for the case with a pitch angle of 0, 30, 45 degrees is 0.361, 0.223, and 0.165, respectively. Similarly, the local loss coefficient for the case with a pitch angle of 0, 30, 45 degrees is 0.879, 0.543, and 0.400, respectively. I would like to highlight that increasing the pitch angle from 0 degree to 45 degrees, the loss coefficient is reduced by more than 50%.

Therefore, I would like to conclude that the pitch angle is an important factor and in the range of parameters considered herein increasing pitch angle would dramatically reduce the loss coefficient, in another word, increase the flow rate with the same pressure gradient.

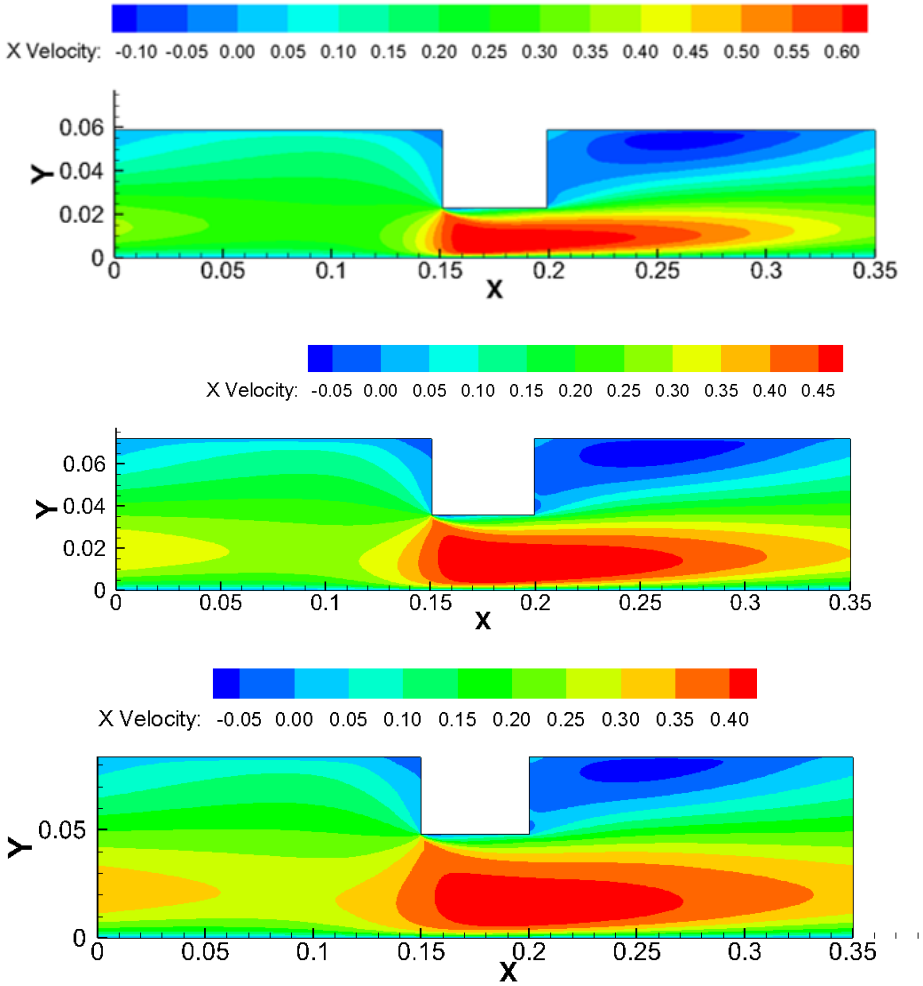

Figure 3.26: Contour of streamwise velocity for case B-6, B-1 and B-7 with air-gap height as 0.023 m, 0.036 m, 0.048m, respectively.

In figure 3.26, I examined the contour of streamwise velocity for B-6, B-1 and B-7. All three cases are with the same bulk velocity 0.2 m/s, the same temperature difference and the same 0 degree pitch angle. I only adjust the height of air gap from 0.023 to 0.048. As shown in the contour plot, the channel height increases from case B-6 to B-7. First, no qualitative difference is observed concerning the velocity distribution. However, the height of air-gap plays an important role in the friction coefficient and local loss coefficient, which are strongly reduced by increasing the air-gap height. For instance, the case of B-6 with air-gap height 0.023 gives local loss coefficient as 1.196 but B-7 with air-gap height 0.048 has a local loss coefficient 0.7, which leads to a more than 40% reduction. The trend observed in present study is in a good agreement with the experiment measurement by Gullbrekken et al. (2017)

As another important factor, I would like to emphasize that the height of air-gap is essential and increasing the air-gap height is helpful to advance the performance of a ventilated roof.

3.3 Channel Flow with Round-Edged Battens

Based on the knowledge learned in Section 3.3, I move on to investigate the flow in the channel with round-edged battens. The effects of batten shape and air-gap height are examined on the flow friction and other physical quantities, such as velocity and temperature distribution. As a validation, some of the current numerical results are compared with the experimental measurements by Gullbrekken et al. (2017).

The motivation of studying such flow configuration is from the practical case of a ventilated pitch roof as shown in figure 3.27. In order to reduce the flow resistance, Gullbrekken et al. (2017) carried out the experiments of a roof model and tested the cases of both sharp-edged battens and round-edged battens. Their results indicate that the round-edged batten with a radius of 0.003 m at the batten corner can efficiently reduce local loss coefficient.

Following the pioneering work by Gullbrekken et al. (2017), in this Section, I use the CFD tool to examine the effect of batten shape on the flow friction, in which I study three different types of round-edged battens. Moreover, I examine the effect of air-gap height in such a flow configuration. By means of CFD, I also look into the flow contour with lots of details, which cannot be provided by experiments.

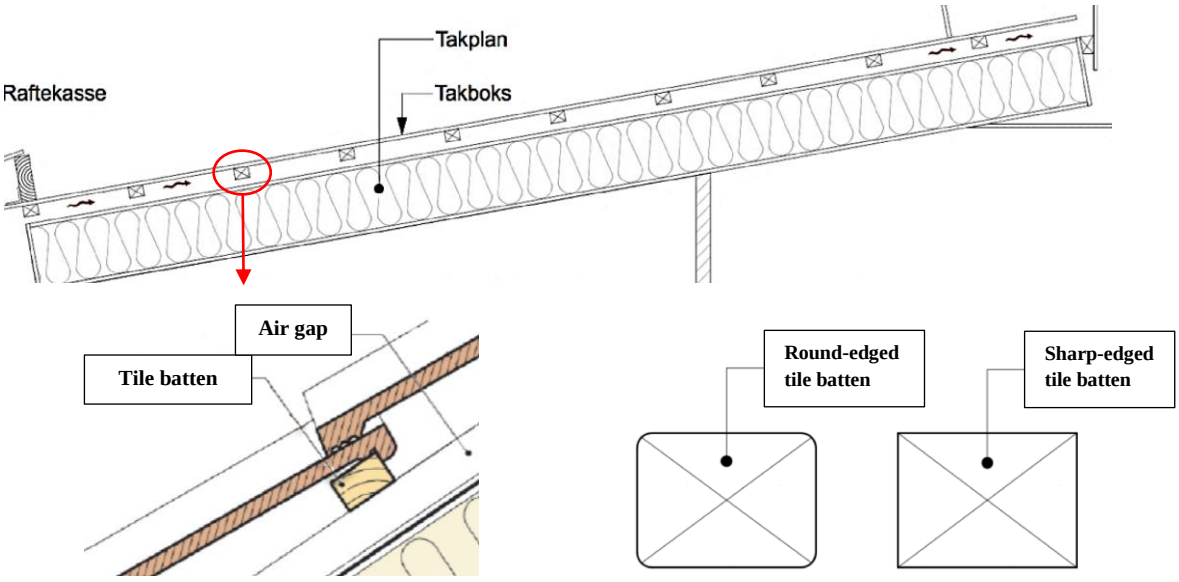

Figure 3.27: Sketch of ventilated roof and the shape of round-edged batten and shape-edged batten (Gullbrekken et al. 2017).

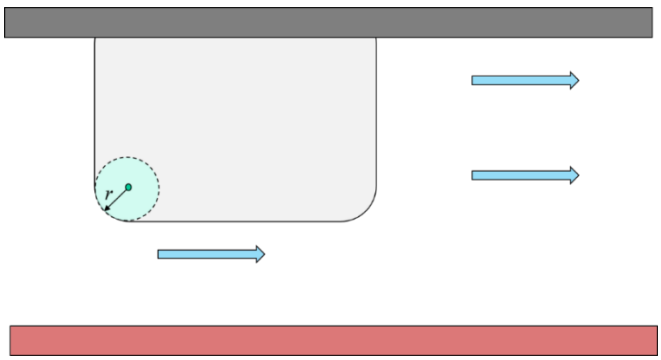

Figure 3.28: A round-edged tile batten with a radius *r*.

3.3.1 Grid-dependence test

Actually including battens makes the geometry of the computation model more complicated than the earlier cases in Section 3.1 and 3.2, mainly due to the shape of round-edged battens. The main difficulty is how to generate high quality Cartesian mesh for such flow configuration.

Because of the round corner of the batten, it is easier to generate the Cartesian mesh in O-block shape as shown in figure 3.29 (b). To check the quality of O-block mesh, I generated two types of mesh as shown in figure 3.29. I select a case of channel flow with sharp-edged battens for testing. The detailed parameters of this case BR-1 can be found in table 3.9. I compared the pressure gradient by using the two different meshes and as shown in table 3.7, the two meshes give similar results and the difference is about 5%. Therefore, in the rest simulations I use the O-block mesh.

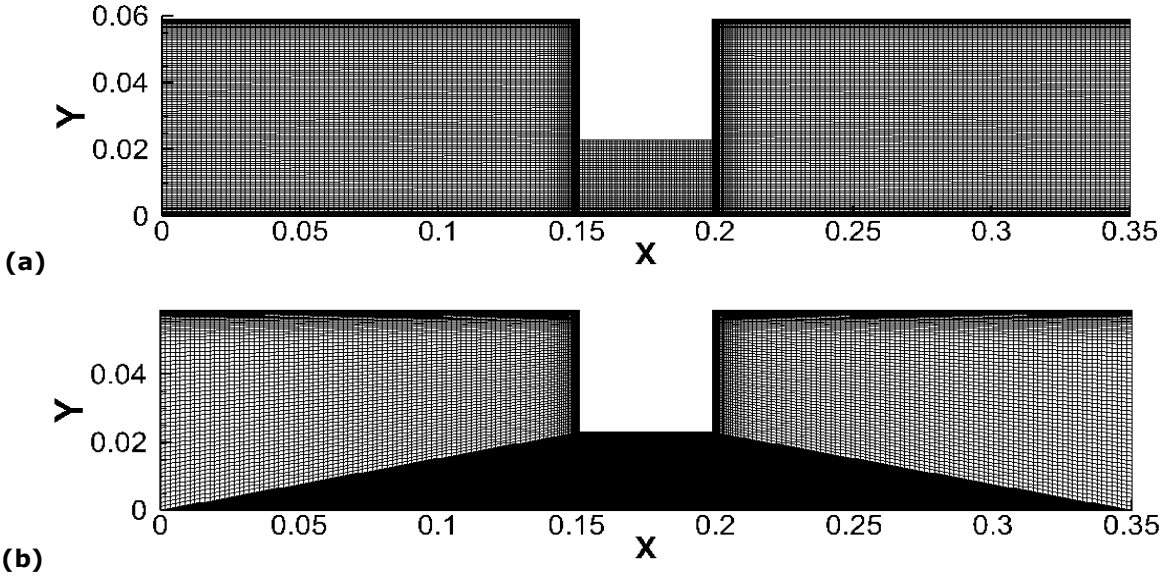

Figure 3.29: BR-1 mesh type comparison. (a) a regular mesh, and (b) O-block mesh.

Table 3.7:Test of regular mesh and O-block mesh.

Case	Regular mesh	O-block mesh
Pressure gradient of BR-1	-0.5510	-0.5215

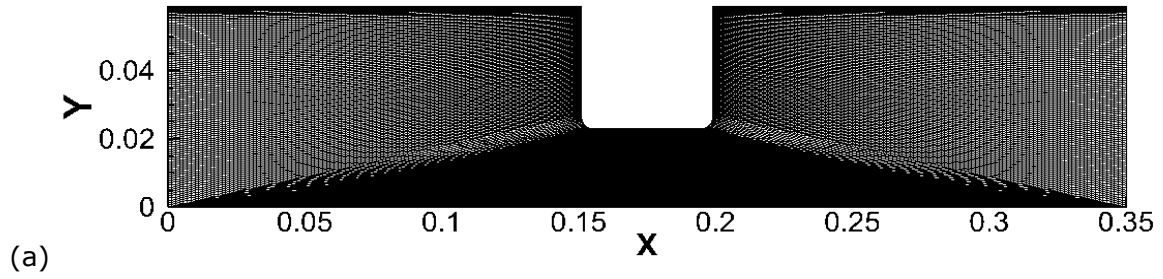

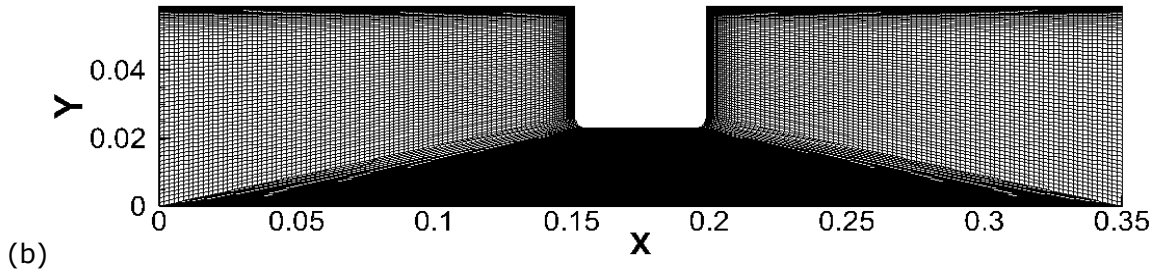

(b)

Figure 3.30: BR-6 mesh resolution comparison. (a) Mesh I and (b) Mesh II.

Table 3.8: Test of grid resolution independence.

Case	Mesh I	Mesh II
Grid nodes	21800	38160
Pressure gradient of BR-6	-0.4385	-0.4368

Furthermore, I test the grid-dependence of O-block by comparing two meshes with different resolutions. As shown in table 3.8, Mesh I has 21800 grid nodes and Mesh II has 38160 grid nodes and a direct comparison is made in figure 3.30. As we can see, the two different meshes give almost the same pressure gradient in the case of BR-6 (see table 3.9 for detailed case parameters), which is a case of channel flow with round-edged battens. Therefore, the Mesh I seems sufficiently reliable with respect to the grid-dependence. In the following numerical study, I keep using Mesh I.

3.3.2 Effects of air gap and round-edged shape of battens

To investigate the effect of the round-edge shape of battens and the air-gap height, I designed 20 cases and summarized the detailed parameters in table 3.9. The first five cases from BR-1 to BR-5 are the references of sharp-edged batten flow with different heights of air gap H_a. For the case BR-6 to BR-10, the batten is round-edged and the radius r of the corner is 0.004 m and then increases to 0.008 m for BR-11 to BR-15, and 0.012 m for the case of BR-16 to BR-20. Note that all cases are with the same temperature difference 10 *K* and the same pitch angle 0 degree. In addition, the size of batten is fixed as 0.036 × 0.048 m.

Similar to Section 3.2, here I employ the κ-ε two-equation turbulence model with standard wall function. The momentum and energy conservation equations are solved using a second-order upwind scheme. The equations of turbulent kinetic energy and dissipation rate are integrated using a first-order upwind scheme.

Table 3.9: Simulation parameters of channel flow with battens and the size of batten is 36*48 mm.

Case ID	Radius of round corner (m)	Mean velocity under battens (m/s)	Ha (m)	Lb (m)	Pressure gradient	Friction coefficient	Local loss coefficient
BR-1	0.00	0.513	0.023	0.35	-0.551	0.663	1.196
BR-2	0.00	0.400	0.036	0.35	-0.247	0.362	0.881
BR-3	0.00	0.350	0.048	0.35	-0.150	0.258	0.702
BR-4	0.00	0.303	0.070	0.35	-0.081	0.176	0.506
BR-5	0.00	0.251	0.140	0.35	-0.038	0.135	0.341
BR-6	0.004	0.513	0.023	0.35	-0.439	0.528	0.952
BR-7	0.004	0.400	0.036	0.35	-0.202	0.297	0.721
BR-8	0.004	0.350	0.048	0.35	-0.125	0.214	0.583
BR-9	0.004	0.303	0.070	0.35	-0.070	0.151	0.435
BR-10	0.004	0.251	0.140	0.35	-0.027	0.095	0.240
BR-11	0.008	0.513	0.023	0.35	-0.410	0.493	0.890
BR-12	0.008	0.400	0.036	0.35	-0.193	0.283	0.688
BR-13	0.008	0.350	0.048	0.35	-0.122	0.208	0.567
BR-14	0.008	0.303	0.070	0.35	-0.068	0.148	0.426
BR-15	0.008	0.251	0.140	0.35	-0.026	0.093	0.235
BR-16	0.012	0.513	0.023	0.35	-0.386	0.464	0.837
BR-17	0.012	0.400	0.036	0.35	-0.184	0.271	0.659
BR-18	0.012	0.350	0.048	0.35	-0.118	0.202	0.549
BR-19	0.012	0.303	0.070	0.35	-0.067	0.145	0.417
BR-20	0.012	0.251	0.140	0.35	-0.026	0.092	0.231

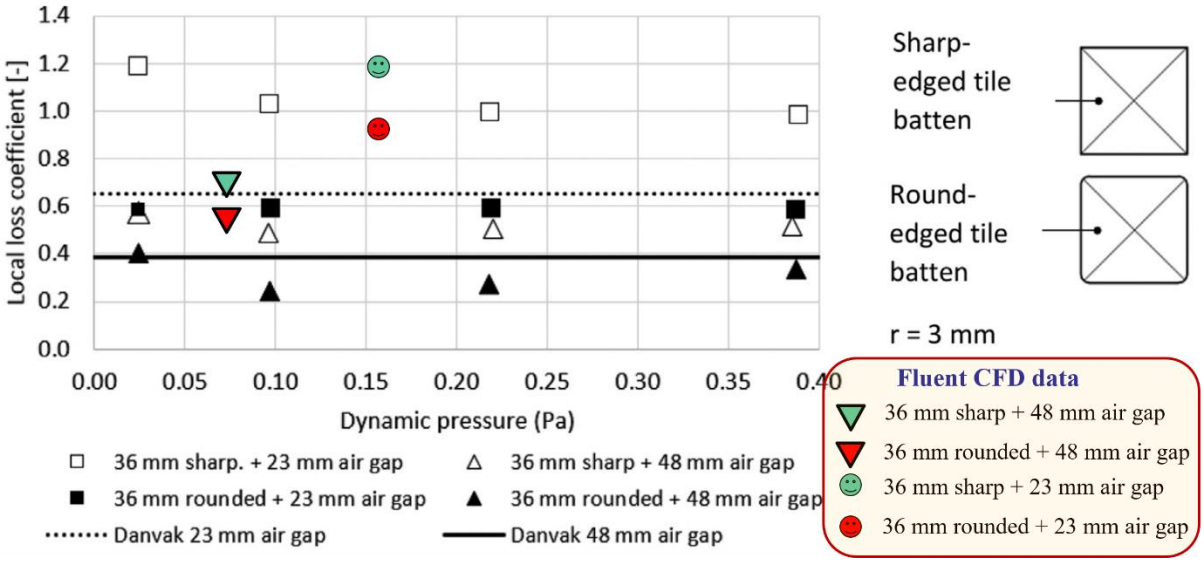

Figure 3.31: Local loss coefficient for sharp-edged and rounded battens with different air gaps and dynamic air pressure. 'Danvak' means values are from Hansen et al. (2013). The colorful symbols are the CFD data from the present study. The figure is made based on the original figure from Gullbrekken et al. (2017).

First of all, I follow the study by Gullbrekken et al. (2017) and compared my CFD results with their experimental data as shown in figure 3.31 that I put 4 data points of my results on the figure in Gullbrekken et al. (2017). The green and red circles represent my results of sharp and rounded-edged batten with a 0.023 m air gap, respectively, and they are comparable with the experimental results of the open and filled squares. Similarly, the green and red gradient symbols stand for my results of sharp and rounded-edged batten with a 0.048 m air gap, respectively, and they are comparable with the experimental data of the open and filled triangles. The discrepancy of the magnitude between the current numerical results and experimental data can be due to the numerical accuracy of the scheme or the limitation of the turbulence model used in the present study. However, both numerical results and experimental data are qualitatively consistent and in the same order. The consistent trends can be seen that the round-edged batten case has a lower local loss coefficient and with increasing the height of air-gap the loss coefficient reduces, which has been also observed in Section 3.2.

Based on the comparison made in figure 3.31 and the above discussion, I am now confident with the reliability of the current numerical simulations and I move on to examine more detailed quantities in the following pages.

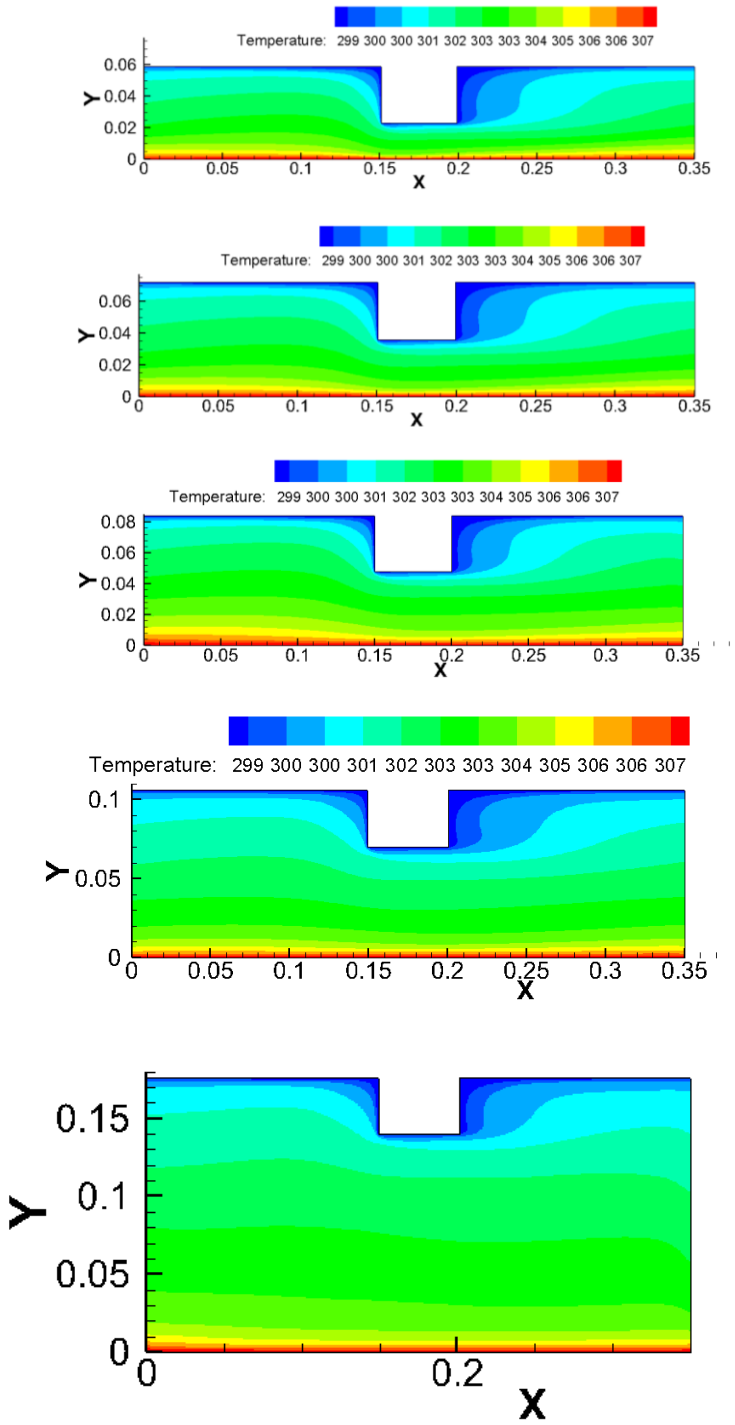

Figure 3.32: Contour of temperature of case BR-1 to BR-5 (From top panel to bottom panel).

Figure 3.32 shows the contour of the first five cases in table 3.9. The cases of BR-1 to BR-5 are with sharp-edged battens and the air-gap height increases from 0.023 m to 0.14m.The flow becomes more like to the channel flow with a smooth wall by increasing the height of air gap. In another word, the influence of batten is weakened by increasing the air-gap height. The influence on the temperature distribution can be seen at the bottom wall, where the temperature is higher. The temperature distribution becomes uniform with increasing the air-gap height because the relative height of batten to the channel height is reduced.

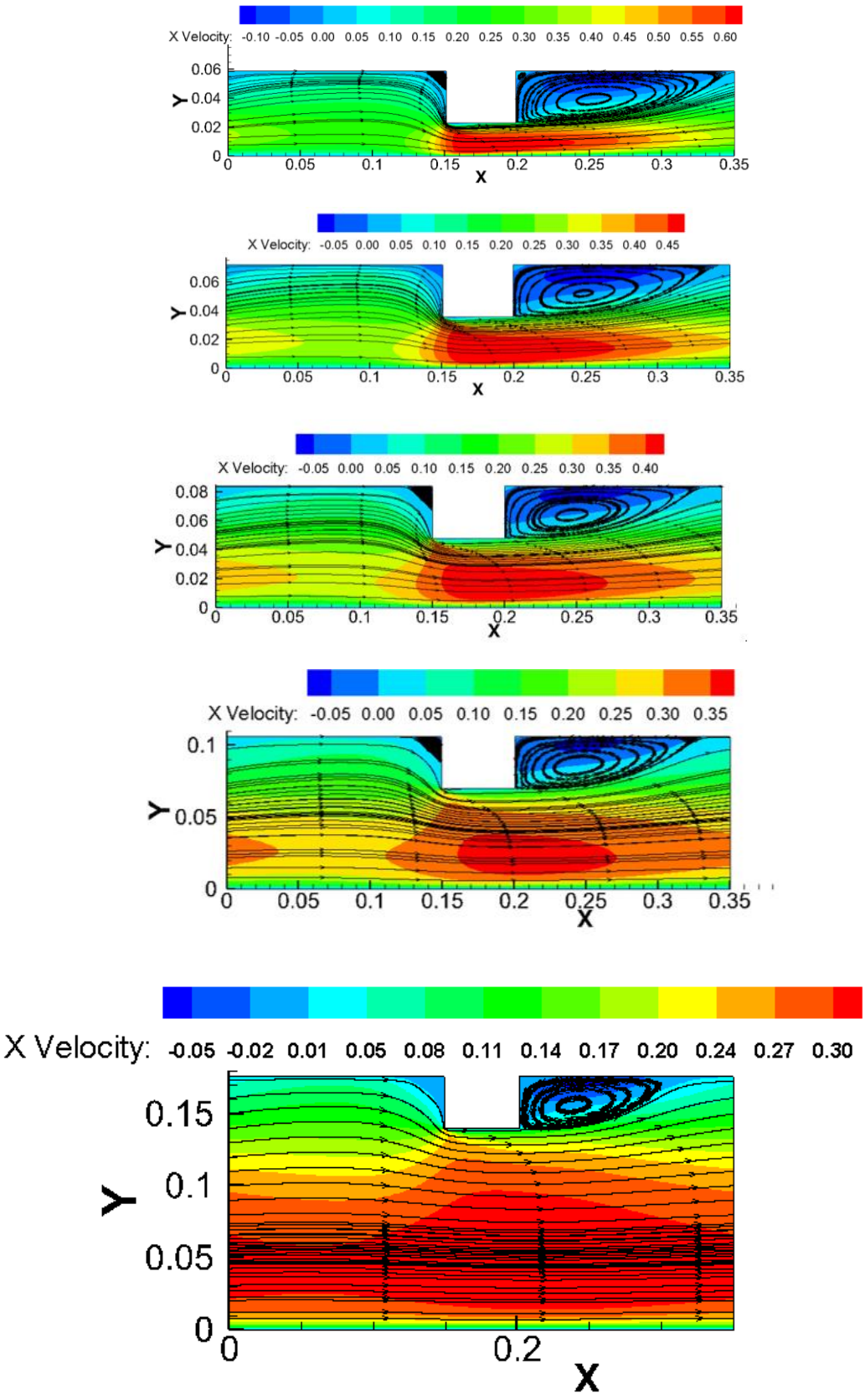

Figure 3.33: Contour of the streamwise velocity of case BR-1 to BR-5 with streamlines.

Following the earlier figure 3.32, I move on to examine the effect of air-gap height on the distribution of airflow velocity in figure 3.33. It is clear that the velocity distribution becomes uniform with increasing the air gap that the lower half of the case BR-5 is identical to the laminar flow. Again, those results reveal that the influence of batten on the flow field gradually attenuates as the height of air gap grows.

I also compute the friction coefficient and local loss coefficient for the case BR-1 to BR-5 (see table 3.9). Consistent with the experimental observation by Gullbrekken et al. (2017), the flow loss coefficient reduces from 1.196 (BR-1) to 0.341 (BR-5) as the air-gap grows. This significant reduction can be understood because the form drag contribution to the total flow resistance is reduced with increasing the air-gap.

As a summary, with a fixed flow rate the increase of air gap can be helpful to reduce the loss coefficient and make the airflow pass through the channel more efficiently.

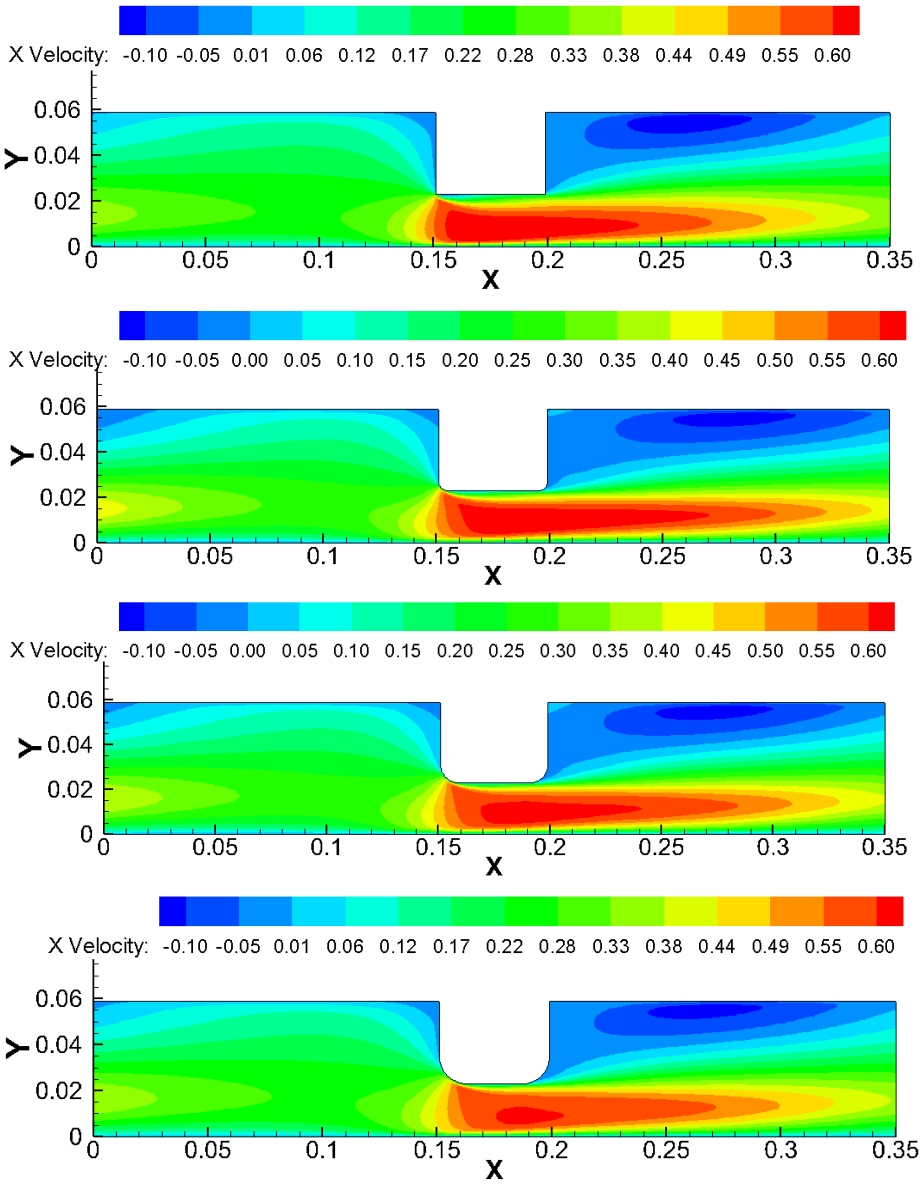

Figure 3.34: Contour of streamwise velocity of the cases BR-1, BR-6, BR-11, and BR-16 (from the top panel to the bottom panel).

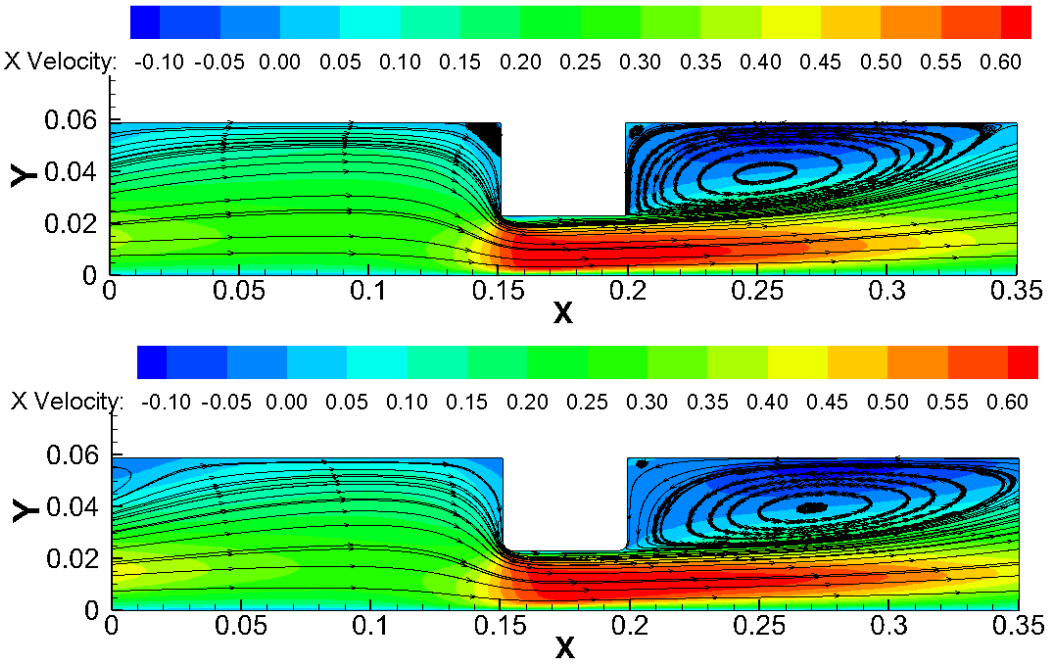

Figure 3.35: Comparison of the velocity contour and streamline pattern of BR-1 and BR-6.

The shape effect of batten on the flow behavior is examined in figure 3.34 and 3.35. First, I compare the contour of streamwise velocity for the case BR-1, BR-6, BR-11 and BR-16 corresponding to the radius *r* of batten corner as 0 m, 0.004m, 0.008m and 0.012 m (see table 3.9). The increase of radius *r* stands for a rounder edge. The general flow pattern shown in figure 3.34 is similar for all cases but the vortex region (blue region) behind the batten is shifted toward the downstream with a round edge and with increasing the radius *r*. To confirm this observation, I plot the streamlines for the case BR-1 and BR-6 in figure 3.35 and it is clear that the core of circulation is shifted toward downstream with a round edge.

What is the implication for the friction factor and loss coefficient? As shown in table 3.9, with increasing the radius of round corner, both the friction factor and loss coefficient are reduced. It is interesting to see that the reduction of friction loss is significant from the case BR-1 with sharp-edged battens to the case BR-6 with slightly round-edged battens. The reduction becomes less significant if I increase the radius more from the case BR-6 to BR16 (r = 0.012 m).

This observation is interesting and meaningful for the design of ventilated roof. To have the airflow passing the roof channel efficiently, i.e. low flow resistance, making slightly round-edged batten is a useful method. Moreover, it is not necessary to make the batten very round, which can keep the strength of batten.

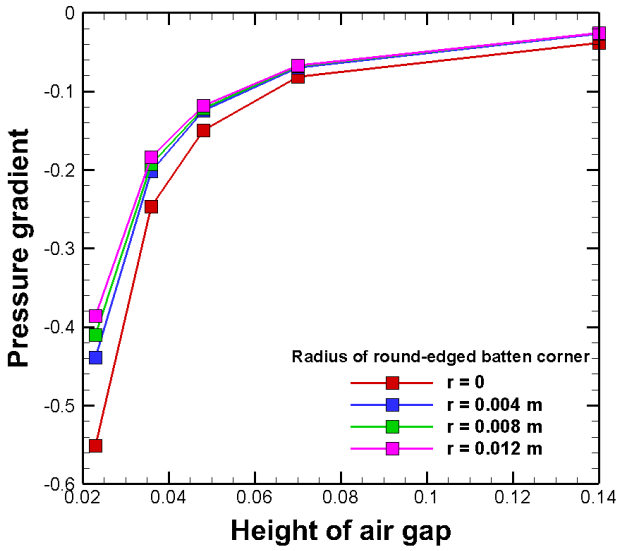

(a)

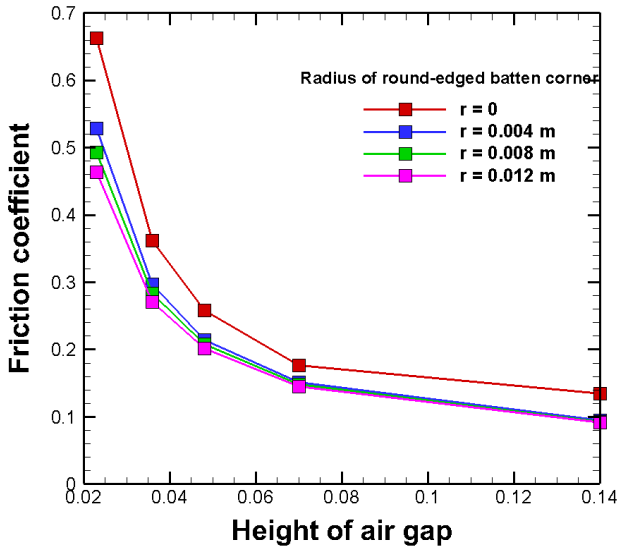

(b)

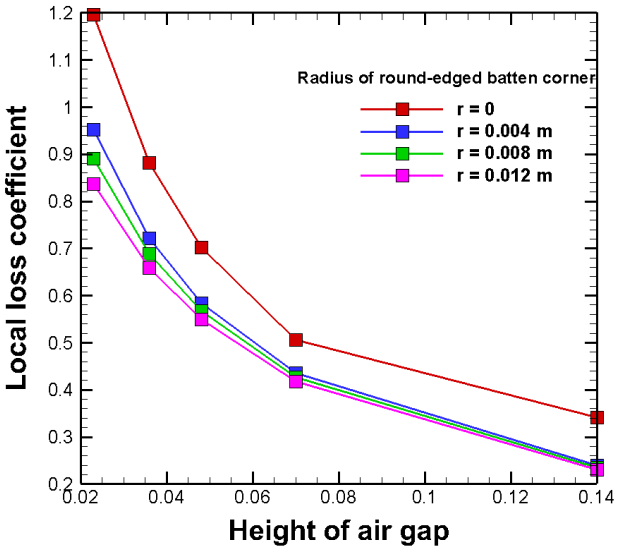

. (c)

Figure 3.36: Effect of air gap height on (a) the pressure gradient, (b) friction coefficient, and (c) local loss coefficient.

As discussed in the earlier text, the air-gap height and roundness of batten are two factors that are essential on the flow friction and worthy of deeper analysis. I compute the mean pressure gradient, friction coefficient and local loss coefficient for all 20 cases and quantitatively examine the dependence of those physical terms on the two factors.

As shown in figure 3.36a, I first plot the pressure gradient versus the height of air gap for the cases grouped with different roundness. The plot clearly shows that the pressure gradient monotonically reduces as the air gap grows. I find a quick reduction of pressure gradient with increasing the air gap from 0.023 m to 0.048 m and then the reduction is slow down from air gap 0.048 m to 0.14 m. The figure 3.36b and 3.36c show the friction coefficient versus the air-gap height and local loss coefficient versus the air-gap height, respectively. Both panel show a similar trend that both friction coefficient and local loss coefficient are monotonically reducing with increasing the air gap. This observation is in agreement with the experimental measurement by Gullbrekken et al. (2017). Similarly, the reduction is significant from air gap 0.023 m to 0.048 m and then the reduction level is weakened from 0.048 m to 0.14 m. On the other hand, the roundness of batten shows an essential effect on the flow friction and local loss coefficient, which are monotonically attenuated with increasing the roundness. Therefore, in the view of flow resistance reduction, increasing the air gap is an effective approach but this approach works nicely only in the range of air gap from about 0.023 m to 0.048 m.

Furthermore, I examine the effect of batten roundness on the pressure gradient, friction coefficient and local loss coefficient in figure 3.37. First, the pressure gradient monotonically decreases as the roundness grows, i.e. the radius of round corner increases. Moreover, the gradient of increase is maximum from sharp-edged case to the slightly round-edged case, i. e. the radius of the corner is 0.004 m. Then the increase is slow down with increasing the batten roundness. As for the friction coefficient and local loss coefficient, the increase of batten roundness (the radius of corner) reduces the friction and local loss as shown in figure 3.37 (b) and (c). The reduction is most significant from a sharp-edged case to a slightly round-edged case. This observation is consistent with the experimental measurement by Gullbrekken et al. (2017). Based on these results, using round-edged batten in the ventilated roof application is a useful way to reduce the airflow friction, in another word, to increase the flow rate at the same flow conditions. Moreover, the slight roundness ($r = 0.004$ m) gives a similar reduction of flow friction as the most rounded case ($r = 0.012$ m). Therefore, it suggests that slightly round-edged batten can be sufficient in practice, which is easier to produce compared with the most round-edged case.

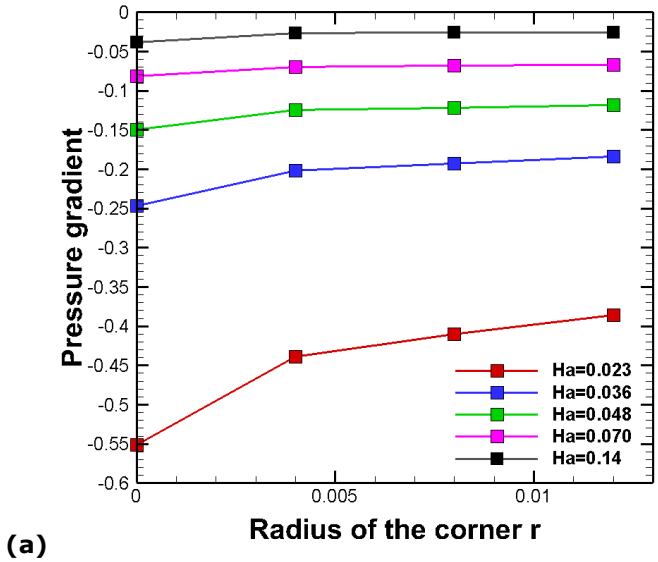

(a)

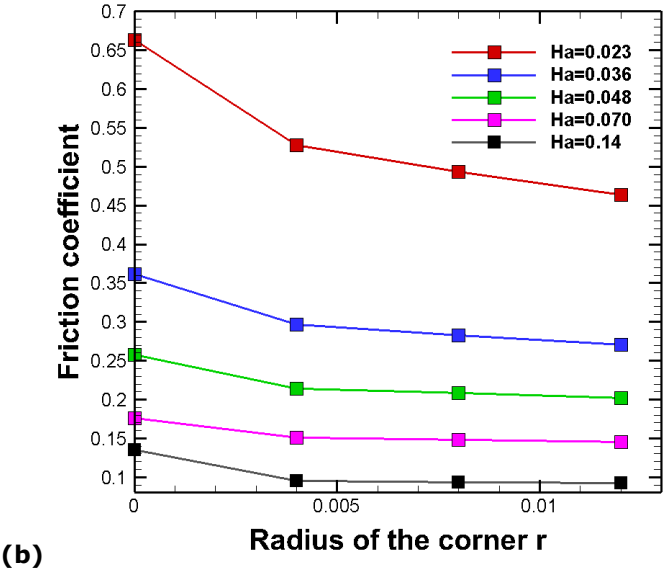

(b)

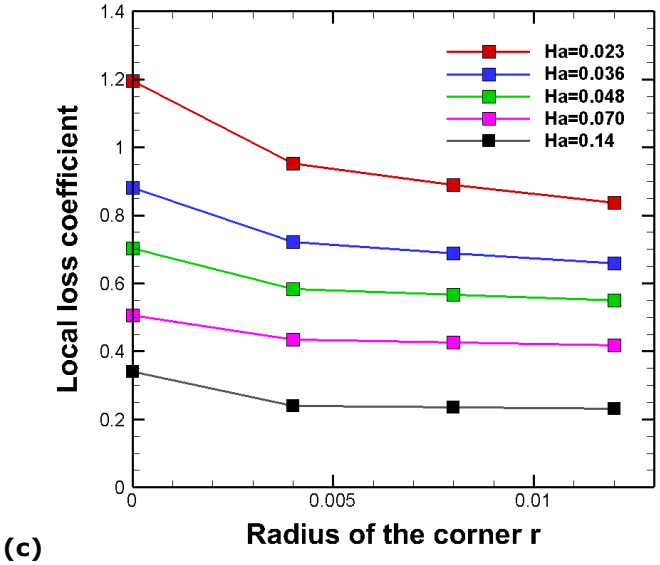

(c)

Figure 3.37: Effect of radius of batten round-edge on (a) the pressure gradient, (b) friction coefficient, and (c) local loss coefficient.

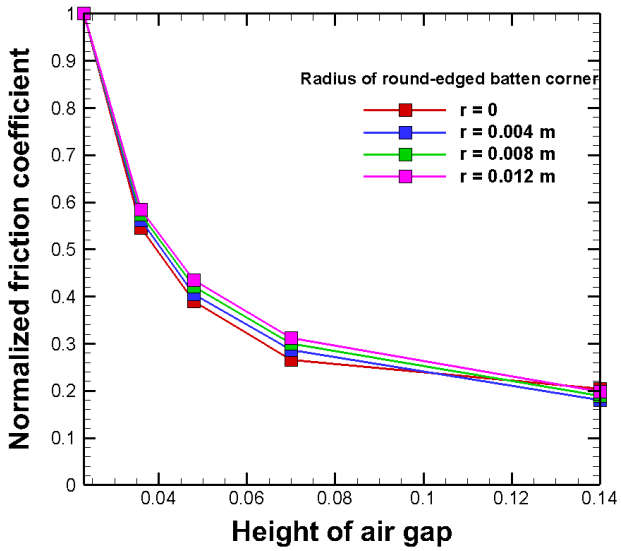

Figure 3.38: Effect of air gap height on the normalized friction coefficient.

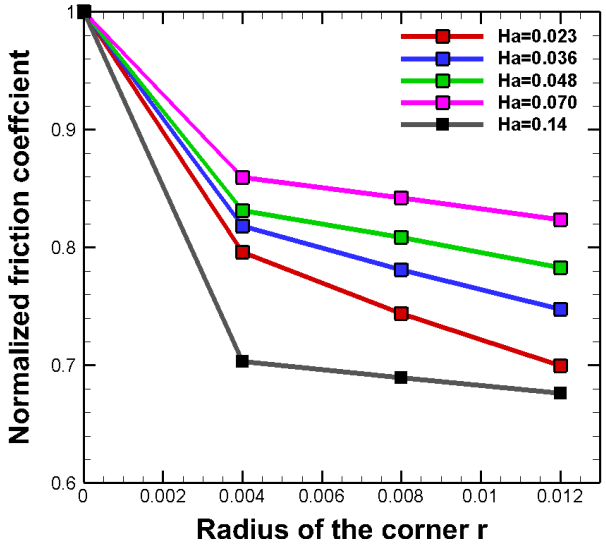

Figure 3.39: Effect of radius of batten round-edge on the normalized friction coefficient.

Furthermore, to evaluate how much percentage of the reduction for the friction coefficient, I normalize the friction coefficients by using the value of friction coefficient of the sharp-edged case (r = 0 m). Figure 3.38 shows the normalized friction coefficient versus the height of air gap and it is interesting to see that all curves are collapsed together. This observation indicates that with a certain air-gap height, the reduction of friction coefficient relative to the sharp-edged case is almost the same for all cases even with different batten roundness.

Figure 3.39 shows the normalized the friction coefficient versus the batten roundness. Again, this plot confirms that the reduction is most significant from the sharp-edged case to the slightly round-edged case (r = 0.004 m). Second, the curves are non-monotonically ordered with varying the height of air gap. The pink line with H_a = 0.07 m is on the top indicates the lowest reduction relative to the sharp-edged case. The most effective case is the case with the largest air gap H_a = 0.14 m. The other curves are in the between. This finding implies that we should avoid using the height of air gap H_a = 0.07 m in practice.

3.3.3 Effects of inlet and outlet

Finally, to understand how the airflow behaves at the inlet and outlet, where the battens are absent, I perform a test with the boundary condition of inflow inlet and outflow outlet. In addition, I extend the channel length approaching the outlet boundary. The simulation conditions are similar to the case of BR-2 (see table 3.9).

In figure 3.40, I find that the velocity distribution near the battens is similar to earlier results. However, as we can see that in the inlet region and outlet region the flow looks similar to the flow case of channel with smooth walls in Section 3.1. The influence of battens gradually diminishes in the downstream and flow slowly recovers to a planar channel flow. On the other hand, the bottom panel shows that heat transfer is enhanced in the downstream region, where the battens are absent.

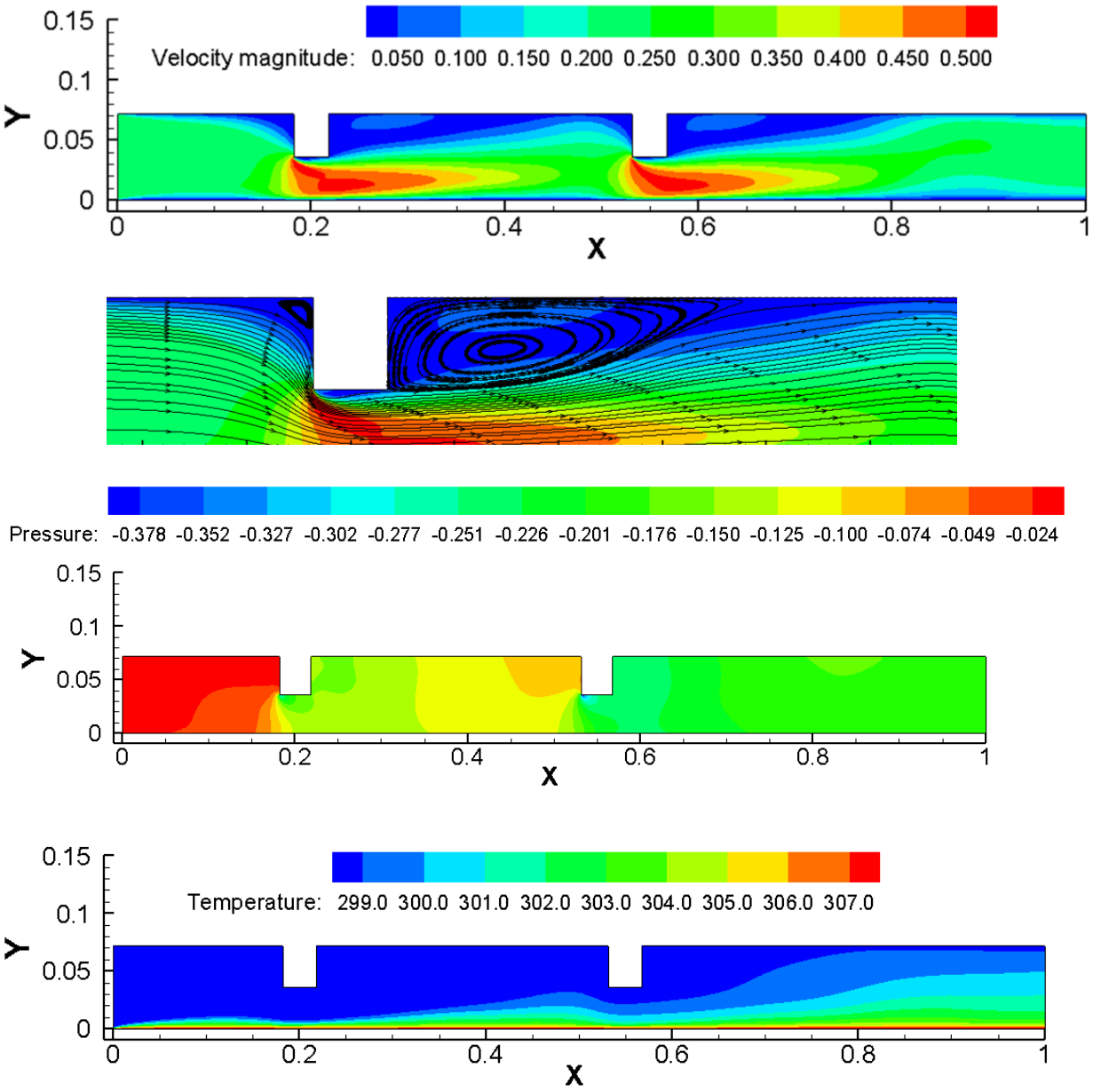

Figure 3.40: Contour of streamwise velocity, static pressure and temperature for the case BR-2 with inflow inlet and outflow outlet boundary conditions.

4 Conclusions and Future Work

4.1 Conclusions

The present thesis numerical studied the airflow passing through the ventilation layer of the pitched wooden roofs, in which various factors such as natural convection induced by the temperature difference of insulation surface and roofing, the pitch angle of the roof, surface roughness of tile battens, have been examined. Following the laboratory model that experimentally tested by Gullbrekken et al. (2017), more than 40 CFD simulations are designed and performed by means of ANSYS Fluent. Both planar channel flow with smooth walls and with tile battens are studied.

First of all, the numerical results are compared with the theoretical values and experimental data (Gullbrekken et al. 2017) and reasonably good agreements are obtained, which reveals that the numerical approach works fine for the current problems and the results are reliable. Based on the results, a detailed further analysis is done with more attentions to the effects of air-gap height and the effect of shape of round-edged tile battens on the pressure gradient, friction coefficient and local loss coefficient. I observe that the pressure gradient monotonically reduces as the air gap grows, which is consistent with experimental measurement by Guillbrekken et al. (2017). A significant reduction of pressure gradient with increasing the air gap from 0.023 m to 0.048 m is observed but the reduction is slow down from air gap 0.048 m to 0.14 m. Similarly, the friction coefficient and local loss coefficient are monotonically attenuated with increasing the air gap. The reduction is significant from air cavity 0.023 m to 0.048 m and then the reduction level is weakened from 0.048 m to 0.14 m.

On the other hand, the roundness of tile batten shows a nontrivial effect on the airflow. First I find the pressure gradient monotonically decreases as the roundness grows, i.e. the radius of tile batten's corner increases. Moreover, the increase of pressure gradient is maximum from sharp-edged case to the slightly round-edged case (the radius of the corner is 0.004 m). Then the increase is slow down with further increasing the tile batten roundness. As for the friction coefficient and local loss coefficient, the increase of tile batten roundness (the radius of corner) greatly reduces the friction and local loss coefficient. The reduction is most significant from a sharp-edged case to a slightly round-edged case.

Based on the findings in present thesis, in the view of flow resistance reduction, increasing the air gap is an effective approach but this approach works efficiently only in the range of air gap from about 0.023 m to 0.048 m in the parameter range considered in present work. Moreover, using round-edged tile battens in ventilated pitched wooden roof application is a useful way to reduce the airflow friction, in another word, to increase the flow rate at the same flow conditions. Surprisingly, a slight roundness ($r = 0.004$ m) gives a significant reduction of flow friction (about 20%). Therefore, it suggests that using a slightly round-edged tile batten, which is easier to produce compared with the most round-edged case, might be sufficient in practical application of ventilated pitched wooden roof.

4.2 Future work

A deep understanding of the flow phyiscs in the ventilated pitched wooden roof is essential for improving the design the this kind of wooden building and control the deficts. This thesis demotrates the portential of CFD simulations applied in this field and the simulations can not only provides the details of the flow structure and temperature difference, but also are ecomonocally efficient compared with experimental tests.

Regarding the future work, because of the time contraint of the Master thesis work, there are other parameters awaiting for further analysis, including the height of tile battens, different temperatures on the roofing, other shaped tile battens, etc. Moreover, as mentioned ealier, the CFD simulations use RANS models and in the future work more expensive numerical approaches, such as Large-Eddy simulation (LES) or even Direct Numerical Simulations (DNS), can be applied in the present problem and those expensive numerical approaches would need much more computing power but will also provide more accurate numerical results, for instance, DNS is turbulence-model free and so-called *numerical experiment*. With sufficient computing resouces, another possible future investigation is performing a full-scale CFD simulation of the whole roof, which could provide a complete picture and all details of the airflow motions in the air cavity.

Reference

Ashrafian, Alireza, Helge I. Andersson, and Michael Manhart. DNS of turbulent flow in a rod-roughened channel. *International Journal of Heat and Fluid Flow* 25 (2004), 373–83.

Barna, I. F., M. A. Pocsai, S. Lökös, and L. Mátyás. Rayleigh–Bènard Convection in the Generalized Oberbeck–Boussinesq System. *Chaos, Solitons & Fractals* 103 (2017): 336–41.

Boussinesq, J. (1903). Thōrie analytique de la chaleur mise en harmonie avec la thermodynamique et avec la thōrie mcanique de la lumi_re: Refroidissement et chauffement par rayonnement, conductibilit des tiges, lames et masses cristallines, courants de convection, thōrie mcanique de la lumi_re. Gauthier-Villars.

Bunkholt, Nora Schjøth, Toivo Säwén, Martina Stockhaus, Tore Kvande, Lars Gullbrekken, Paula Wahlgren, and Jardar Lohne. Experimental study of thermal buoyancy in the cavity of ventilated roofs. *Buildings* 10, (2020): 8.

Bunkholt, Nora Schjøth. Eksperimentell studie av termisk oppdrift i tak med luftet tekning. Master thesis, Norwegian University of Science and Technology (2019).

Bøhlerengen, T. Isolerte skrå tretak med lufting mellom vindsperre og undertak. *In SINTEF Building Research Design Guides* 525.101; SINTEF: Oslo, Norway (2007).

Bøhlerengen, T. Isolerte skrå tretak med kombinert undertak og vindsperre. *In SINTEF Building Research Design Guides* 525.102; SINTEF: Oslo, Norway (2012).

Djenidi, L., Elavarasan, R., Antonia, R.A. The turbulent boundary layer over transverse square cavities. *J. Fluid Mech*. 395 (1999), 271–294.

Edvardsen, K.; Ramstad, T. Trehus Håndbok 53. *SINTEF Building and Infrastructure*, Norway (2006).

Edvardsen, K.; Ramstad, T. Trehus Håndbok 5. *SINTEF Building and Infrastructure*, Norway (2014).

Espen, Hansen. Luftstrømning i skrå tretak. *Master thesis*, Norwegian University of Science and Technology (2016).

Eggen, Martin Grimstad and Røer, Olaf Vemmestad. Lufting av skrå tretak - Trykktap ved ulike luftespalteutforminger. *Master thesis*, Norwegian University of Science and Technology (2018).

Gullbrekken, L. Climate Adaptation of Pitched Wooden Roofs. Ph.D. thesis, Norwegian University of Science and Technology (2018).

Gullbrekken, L.; Kvande, T., Jelle, B.P. and Time, B. Norwegian pitched roof defects. *Buildings* 6 (2016), 24.

Gullbrekken, Lars, Sivert Uvsløkk, Stig Geving, and Tore Kvande. Local loss coefficients inside air cavity of ventilated pitched roofs. *Journal of Building Physics*, 42 (2017): 197-219.

Gullbrekken, Lars. Ventilated wooden roofs: influence of local weather conditions – measurements. In: NSB 2017 – *11th Nordic symposium on building physics* (2017), Trondheim.

Grynning, Steinar, Silje Kathrin Asphaug, Lars Gullbrekken, and Berit Time. Moisture robustness of eaves solutions for ventilated roofs: experimental studies. *Science and Technology for the Built Environment* 25 (2019): 1121–31.

Furuya, Y., Miyata, M. & Fujita, H. Turbulent boundary layer and flow resistance on plates roughened by wires. *Trans. ASME: J. Fluids Engng* 98 (1976), 635–644.

Kim, John, Parviz Moin, and Robert Moser. Turbulence statistics in fully developed channel flow at low Reynolds number. *Journal of Fluid Mechanics* 177 (1987): 133–66.

Leonardi, S., P. Orlandi, L. Djenidi, and R. A. Antonia. Structure of turbulent channel flow with square bars on one wall. *International Journal of Heat and Fluid Flow* 25 (2004): 384–92.

Leonardi, S., P. Orlandi, and R. A. Antonia. Properties of d- and k-type roughness in a turbulent channel flow. *Physics of Fluids*, 19 (2007): 125101.

Moody, L. F. Friction factors for pipe flow. *Transactions of the ASME*, 66 (1944): 671–684.

Norwegian Ministry of Climate and Environment. Climate change adaptation in Norway. (2015)

Perry, A. E. and Joubert, P. N. Rough wall boundary layers in adverse pressure gradients.

J. Fluid Mech. 17(1963), 193–211.

Pope, Stephen (2000). Turbulent Flows. *Cambridge University Press*, 1st Edition (2000)

Raupach, M. R. Drag and drag partitioning on rough surfaces. *Boundary Layer Meteorol.*, 60(1992), 375–395.

Raupach, M. R., D. A. Gillette, and J. F. Leys. The effect of roughness elements on wind erosion threshold. *J. Geophys. Res.*, 98(1993), 3023–3029.

Roels S. and Langmans J. Highly insulated pitched roofs resilient to air flow patterns: Guidelines based on a literature review. *Energy and Buildings* 120 (2016): 10-18.

Shawn, W. ANSYS Fluent 17.0 Introduces New User Interface. *Engineering.com*. (2017).

ANSYS Fluent Theory Guide, ANSYS, Inc., 275 Technology Drive Canonsburg, PA 15317 (2013).

Uvsløkk S. Importance of wind barriers for insulated timber frame constructions. Journal of Thermal Insulation and Building Envelopes 20 (1996): 40-62.

Wood, D.H., Antonia, R.A. Measurements of a turbulent boundary layer over a d-type surface roughness. *J. Appl. Mech*. 42 (1975), 591–597.

NTNU

Norwegian University of
Science and Technology